

Diss. ETH No 14144

# **Electron spectroscopy on nanosized particles in a carrier gas**

A dissertation submitted to the  
SWISS FEDERAL INSTITUTE OF TECHNOLOGY ZURICH  
for the degree of  
Doctor of Natural Sciences

presented by  
Alejandro Niels Keller Pérez  
Lic. Ing. Física, UIA  
born October 25th, 1970  
citizen of Mexico

accepted on the recommendation of:  
Prof. Dr. H. C. Siegmann, examiner  
Prof. Dr. D. Pescia, co-examiner

2001



# Contents

Abstract	1
Zusammenfassung	3
Chapter 1. Surface Science with Nanosized Particles in a Carrier Gas	5
1. Introduction	6
2. Evaluation of the surface area	7
3. Chemical fingerprint of the active surface	15
4. Theoretical background of the scaling laws	20
5. Conclusions	24
Chapter 2. Effects of second order processes in aerosol monitoring	27
1. Introduction	28
2. Theory	29
3. Methods	33
4. Results and Discussion	36
Chapter 3. Magnetic circular dichroism in the photoionization of nanoparticles in gas suspension	47
1. Introduction	48
2. Ferrofluids	49

3. Methods	50
4. Results and Discussion	56
5. Conclusions	64
Bibliography	65
Acknowledgements	73
Curriculum vitae	75

# Abstract

The study of nanoparticles suspended in a carrier gas has gained a lot of attention over the last years. The reason for this is not only their increasing amount of applications, that extend to fields as diverse as materials physics, geology, biology, and medicine, but also the well documented effects that nanoparticles originating in combustion processes have on public health. Yet, up to now, disciplines like surface science have largely neglected the study of their characteristics. The purpose of this work is to show that the study of the surface properties of nanoparticles in a carrier gas is a rewarding new field of research with many important applications. In addition, we have also developed methods to study the surface of nanoparticles in applications as general as pollution concentration and as specific as surface magnetism, this last one being the first reported study of the magnetic properties of the surface of nanoparticles suspended in a carrier gas.

In the first chapter, we introduce the concept of active surface. The active surface is the surface on which transfer of momentum, energy, and mass from the gas to the particle takes place. The available experimental data shows that the active surface may be determined in physically very different *in situ* experiments such as measuring the mobility  $b$ , the diffusion constant  $D$ , or the mass transfer coefficient  $K$  of the particle. The concept of the active surface manifests itself in scaling laws  $Kb = \text{const}$ ,  $KD = \text{const}$  and  $Yb = \text{const}$ , found valid over a large range of particle shapes and sizes.  $Y$  is the yield of low energy photoelectrons from the particles upon irradiating the carrier gas with light of energy below the ionization energy

of the carrier gas molecules but above the photoelectric threshold of the particles. While  $K$ ,  $D$ , and  $b$  are independent of the chemical nature of the particles as far as we know today, the simultaneous measurement of  $Y$  provides a chemical fingerprint of the particles and allows one to observe, in combination with pulsed lasers as sources of light, the dynamical changes of the active surface while the nanoparticle is interacting with the carrier gas.

In the second chapter, we present a general-purpose mathematical model for pollution concentration studies. The model is an approximate solution for the time dependence of size distribution that takes into account processes like aerosol coagulation and condensation among others. Our model is validated by representative experiments using standard aerosol monitoring devices that measure light scattering, particle cross section, particle bound polycyclic aromatic hydrocarbons (PPAH) and number concentration, showing an excellent agreement with the experimental data. The results demonstrate that aerosol coagulation has to be taken into account when monitoring aerosol particles. We also show that the simultaneous application of different sensors reveals new information about the physical and chemical properties of the aerosol.

Finally, we present a new method capable of measuring the magnetic circular dichroism (MCD) in the photoionization of aerosol particles. This is the first device reported to be able to measure the magnetically induced optical anisotropy of nanoparticles in gas suspension. The method relies on the photoemission at energies near the threshold and is therefore sensible to the surface magnetization. The experimental setup was tested with magnetic Ni, Co and  $\text{Fe}_3\text{O}_4$  nanoparticles. Ni showed a maximum MCD asymmetry of  $0.253 \pm 0.096\%$ , while no measurable asymmetry was detected for Co and  $\text{Fe}_3\text{O}_4$ . Further analysis with a Scanning Electron Microscope with Polarization Analysis (SEMPA) confirmed that the surface of the Co particles was magnetically inactive.

## Zusammenfassung

In den letzten Jahren haben Nanoteilchen in Trägergasen viel Beachtung gefunden nicht nur aufgrund der zahlreichen Anwendungen in Gebieten wie Materialwissenschaften, Geologie, Biologie und Medizin, sondern auch wegen der bekanntlich schädlichen Auswirkungen, die Nanoteilchen aus Verbrennungsprozessen auf den Menschen haben. Trotzdem wurden bis jetzt Nanoteilchen in Trägergasen in Disziplinen wie der Oberflächenphysik überhaupt nicht berücksichtigt. In dieser Arbeit zeigen wir, dass die Untersuchung von Nanoteilchen in Trägergasen ein interessantes neues Forschungsgebiet mit vielen Anwendungen ist. Ausserdem haben wir zum ersten Mal eine Messung von Oberflächenmagnetismus von Nanoteilchen in einem Trägergas durchgeführt.

Im ersten Kapitel führen wir das Konzept der aktiven Oberfläche ein. Die aktive Oberfläche ist der Teil der Oberfläche, auf den Impuls, Energie und Masse vom Gas auf das Teilchen übertragen wird. Die bereits durchgeführten Experimente zeigen, dass die aktive Oberfläche durch die Messung von verschiedenen physikalischen Grössen *in situ* bestimmt werden kann. Diese physikalischen Grössen sind: die Mobilität  $b$ , die Diffusionskonstante  $D$ , und der Massentransferkoeffizient  $K$  des Teilchens. Das Konzept der aktiven Oberfläche wird in den „scaling laws“ sichtbar:  $Kb = \text{const}$ ,  $KD = \text{const}$  und  $Yb = \text{const}$ , die über einen breiten Grössenbereich und für verschiedenste Formen der Teilchen gültig sind.  $Y$  ist die Ausbeute von niederenergetischen Photoelektronen aus den Teilchen. Dabei benützen wir UV-Licht, dessen Photonenenergie tiefer ist als die Ionisationsenergie des Trägergases,

aber grösser als die Austrittsarbeit des Teilchens.  $K$ ,  $D$ , und  $b$  sind gemäss heutige Wissensstand unabhängig von der chemischen Zusammensetzung der Teilchen.  $Y$  hingegen hängt stark von der Austrittsarbeit der Teilchen ab und somit auch von der Oberflächenchemie. Die gleichzeitige Messung von  $Y$  und der aktiven Oberfläche liefert somit einen chemischen Fingerabdruck der Teilchen.

Im zweiten Kapitel präsentieren wir ein allgemeines mathematisches Modell für Schadstoffkonzentrationen in Gasen. Das Modell ist eine Näherungslösung für die Zeitabhängigkeit der Grössenverteilung des Aerosols, das unter anderem Prozesse wie Koagulation und Kondensation berücksichtigt. Wir haben unser Modell mit Messungen von Anzahlkonzentration, Lichtstreuung, Teilchenoberfläche, und partikelgebundenen polyzyklischen aromatischen Kohlenwasserstoffen (PPAK) überprüft. Die Übereinstimmung zwischen Modell und Experiment ist hervorragend. Die Resultate zeigen, dass man Koagulationsprozesse berücksichtigen muss, wenn man die zeitliche Entwicklung der Eigenschaften von Aerosolen misst. Wir zeigen auch, dass die simultane Messung mit verschiedenen Sensoren zusätzliche Informationen über die physikalischen und chemischen Eigenschaften des Aerosols bringt.

Zuletzt demonstrieren wir eine neue Methode, mit der der magnetische zirkulare Dichroismus (MCD) an Nanoteilchen in der Photoemission gemessen werden kann. Dies ist die erste Messung der magnetisch induzierten optischen Anisotropie von Nanoteilchen in einem Trägergas. Die Methode basiert auf der Photoemission bei Photonenenergien nahe an der Photoschwelle. Aufgrund der kleinen Austrittstiefe der Photoelektronen ist diese Methode nur auf die Magnetisierung der Oberfläche empfindlich. Wir haben das Experiment mit magnetischen Nanoteilchen aus Ni, Co und  $\text{Fe}_3\text{O}_4$  durchgeführt. Bei Ni haben wir eine MCD Asymmetrie von  $0.253 \pm 0.096\%$  gefunden, während bei Co und  $\text{Fe}_3\text{O}_4$  kein Effekt gefunden wurde. Eine Analyse der Co-Teilchen mit einem Rasterelektronenmikroskop mit Polarisationsanalyse (SEMPA) hat gezeigt, dass ihre Oberfläche unmagnetisch ist.



## Surface Science with Nanosized Particles in a Carrier Gas

ABSTRACT. The dynamics of nanoparticles in a carrier gas are governed by the physical and chemical nature of the surface. The total surface area can be divided into an “active” and a “passive” part. The active surface is the surface on which transfer of momentum, energy, and mass from the gas to the particle takes place. The experiments show that the active surface may be determined in physically very different *in situ* experiments such as measuring the mobility  $b$ , the diffusion constant  $D$ , or the mass transfer coefficient  $K$  of the particle. The concept of the active surface manifests itself in scaling laws  $Kb = \text{const}$ ,  $KD = \text{const}$  and  $Yb = \text{const}$ , found valid over a large range of particle shapes and sizes.  $Y$  is the yield of low energy photoelectrons from the particles upon irradiating the carrier gas with light of energy below the ionization energy of the carrier gas molecules but above the photoelectric threshold of the particles. While  $K$ ,  $D$ , and  $b$  are independent of the chemical nature of the particles as far as we know today, the simultaneous measurement of  $Y$  provides a chemical fingerprint of the particles and allows one to observe, in combination with pulsed lasers as light sources, the dynamical changes of the active surface while the nanoparticle is interacting with the carrier gas.

---

\*Published in: A. Keller *et al.*, J. Vac. Sci. Technol. A 19(1), Jan/Feb 2001

## 1. Introduction

Nanosized liquid or solid bodies may remain suspended in a carrier gas for a long time. They are mesoscopic, containing  $10^3 - 10^6$  atoms or molecules, and may exhibit unexpected properties due to their very large surface to volume ratio. Such nanoparticles in a carrier gas have been largely neglected in surface science. Yet it is evident that it would be highly welcome if not urgent to know more about their surface characteristics. Nanoparticles in air, for instance, have moved to the center of attention because of their well documented effect on public health (Peters et al., 2000). They are deposited in the alveoles of the lung, where the defense mechanisms of the human body are weak; in this way, a number of toxic chemicals adsorbed at the nanoparticle surface penetrate into the human body using the nanoparticles as vehicles. Another example is the precipitation forming process in clouds. It depends to a large extent on the presence of nanoparticles acting as condensation nuclei for ice and water. This has a significant influence on the albedo of the earth and on rain and snowfall (Rosenfeld, 2000).

However, none of these phenomena is understood on the atomic level. It is therefore necessary to adapt the techniques developed in surface science to the characterization of the surface of the nanoparticles. It is important to do the investigations while the nanoparticle remains suspended in its carrier gas. Deposition on a substrate and transfer into vacuum may severely alter the surface characteristics of the nanoparticle and, through the action of surface tension, even its shape. The transfer of momentum, energy, and mass from the gas to the particle as well as the heterogeneous chemical reactions and the surface tension are dominated by an atomically thin layer at the surface. The properties of this layer can be subject to significant transformations without changing the particle bulk parameters. It is well known that a fingerprint of the surface as well as its dynamical changes become observable by measuring the photoelectric yield of the particle while it is suspended in its genuine

carrier gas (Kasper et al., 1999a). The surface characteristics often depend on spurious contaminants of the carrier gas and on small changes of the temperature as well as on fine details in the process of nanoparticle production, be it in an internal combustion engine (Matter et al., 1999) or in a volcano (Ammann et al., 1993). It is the purpose of this work to show that surface science with nanoparticles in a carrier gas is possible and a rewarding new field of research with many important applications.

## 2. Evaluation of the surface area

With nanoparticles it is generally not possible to define the geometry by a few simple parameters, such as diameter, surface area, or volume. This arises because nanoparticles may exhibit bizarre shapes with numerous incisions and internal surfaces. But the surface tension may also contract them into perfect spheres, notably if water or other impurities in the carrier gas condense on them, or if the temperature is raised so that the surface atoms become mobile. The electron microscope, in principle a powerful tool to image nanostructures, has its limitations as the nanoparticles may change shape on substrate deposition and on transfer to the vacuum for instance by evaporation of condensates. Yet, one needs to have some measure of the surface area in order to evaluate adsorption and to understand the interaction with the carrier gas.

**2.1. Surface area from the mobility or the diffusion constant.** The most commonly used technique to determine the “size” of a nanoparticle *in situ* relies on the measurement of the mobility  $b$  of the particle in its carrier gas.  $b$  is defined by assuming a linear friction law  $V = bF$  in which a constant drift velocity  $V$  is reached under the action of an external force  $F$ .  $F = eE$  is generated by attaching one elementary electrical charge  $e$  to the particle and bringing it along with the carrier gas into the electrical field  $E$  of a condenser. Nanoparticles of one specific  $b$  can exit through a slit in the condenser and are counted with a condensation nucleus counter.

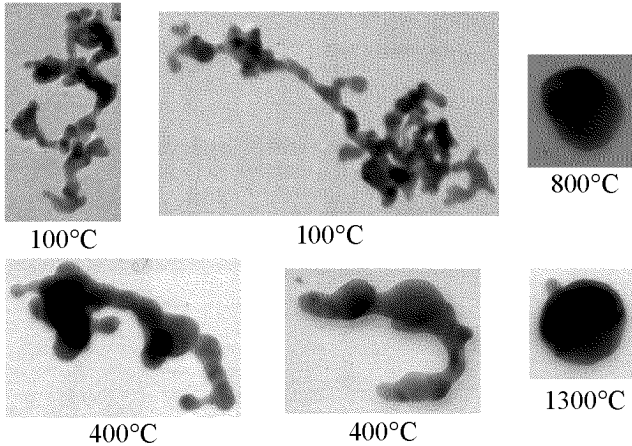


FIGURE 1.1. Electronoptical micrographs of gold particles generated in an electric discharge between gold-electrodes. After the generation, the inert carrier gas has been heated to the temperature indicated. The particles have identical mobilities selected in a differential mobility analyzer. This mobility leads to a mobility diameter  $d_p = 50$  nm which indeed corresponds to the diameter of the spherical particles heated to 800 and 1300°C. The melting point of bulk gold is 1064°C, but it is obvious that the surface atoms become mobile much below that temperature.

By scanning the electric field in the condenser and counting the exiting particles at each field strength, the mobility spectrum of the nanoparticles is obtained.

Figure. 1.1 shows examples of electron micrographs of gold particles that have been generated in an electric discharge between high purity Au electrodes in atmospheric pressure Ar gas which was subsequently heated to the temperature indicated. After that, particles of the mobility  $b = 0.92 \times 10^{-3} \text{ cm}^2/(\text{V s})$  were selected, precipitated on a substrate, and imaged in transmission electron microscopy. For the

simple case of pure Au-particles in pure argon gas, the aforementioned possible distortions by electron microscopy are minimal. Figure 1.1 demonstrates that only those particles heated to high temperatures approximate a spherical shape, the diameter of which turns out to be  $\approx 50$  nm. The “nose” of the particle heated to  $1300^\circ\text{C}$  is probably due to agglomeration with a smaller particle after the heating section but before the mobility analyzer. The generally accepted function connecting the observed mobility with a particle diameter  $d_p$  has been tabulated by Fuchs (Fuchs, 1964). In the case of the particles displayed in Figure 1.1, this function yields  $d_p = 50$  nm as well. However, the unheated Au particles have a much larger geometrical surface area compared to the spherical Au particles. The concept of the mobility diameter clearly can be quite misleading. It is outright wrong to derive the area of the geometrical surface or the volume of the particle from it. Correctly, one has to think of  $d_p$  as a parameter fixing the “active” surface which is essentially the part of the surface that causes the friction in the carrier gas as explained later. The “passive” surface includes the inner surfaces and the surface in bays or incisions that does not interact with the carrier gas.

The theory of the friction coefficient  $1/b$  of a nanoparticle depends on the Knudsen number  $Kn = \lambda/d_p$ , where  $\lambda$  is the mean free path of the carrier gas molecules;  $\lambda = 67$  nm in air at normal conditions. If  $Kn \gg 1$ , one has the molecular particle motion where the gas molecules fly *in vacuo* near the particle. The friction coefficient is then caused by the pressure difference between front and back of the particle yielding:

$$(1) \quad \frac{1}{b} = \frac{1}{3} \pi n m v \delta d_p^2,$$

where  $n$ ,  $m$ , and  $v$  are the density, mass, and average velocity of the gas molecules.  $\delta$  is a factor with value 1.0 or 1.4 depending on whether the reflection of the gas molecules on the nanoparticle is specular or diffuse, respectively. Chemically inert surfaces tend to exhibit specular, chemically active surfaces diffuse reflection. In

actual aerosol practice, the mode of reflection is assumed to be fixed between these two extremes. In reality, it depends on the accommodation coefficient at the interface gas/particle.

For  $Kn \ll 1$ , the particle friction is calculated from fluid dynamics. Assuming spherical particles and very small drift velocity one arrives at the Stokes law in which  $1/b \propto d_p$ . This is the well known paradoxical result that friction depends only on the diameter, not on the cross section of the moving body as long as one has laminar flow. It can be understood qualitatively by considering that friction is effective on those parts of the surface, where the relative velocity component between gas and particle in the direction of motion drops steeply. This reduces the particle surface active in friction to a small strip around the circumference.

For  $Kn \simeq 1$ , one has the transition between molecular and hydrodynamic motion. In many practical applications, this is the regime of interest, yet unfortunately the theory has no rigorous foundation there. It turned out that a velocity slip between gas and moving particle must be taken into account, known as the Cunningham correction factor  $C_c(\lambda/d_p)$ . This function makes it possible to produce a smooth transition between the molecular regime with  $1/b \propto d_p^2$  and the hydrodynamic regime with  $1/b \propto d_p$ . It should be noted that in the molecular regime,  $\frac{\pi}{4}d_p^2$  is the impact cross section averaged over all directions relative to the drift velocity  $V$ . This averaging arises because the particle performs a Brownian rotation.

Hence, the fraction of the geometrical surface that produces friction continually decreases as  $Kn$  decreases, that is as the particle “size” increases. This fraction of the geometrical surface is active in exchanging energy and momentum from the particle to the gas, and we call it therefore the active surface. Inner surfaces, and surfaces in bays or cracks, or with the large particles, surfaces around the front and back dead center of the laminar flow are passive surfaces. The active surface has also been named “Fuchs” surface (Gäggeler et al., 1989).

The diffusion coefficient  $D$  of nanoparticles is measured for instance in diffusion batteries (Hinds, 1982). It is inversely proportional to the same active surface as the mobility  $b$  at constant temperature  $T$  since  $D = kTb$ , where  $k$  is the Boltzman factor.

The mobility and diffusion constant and, hence, the active surface determines the precipitation of nanoparticles in filters. The larger particles tend to be removed by impaction on obstacles in the carrier gas flow such as hairs. This form of particles deposition is governed by the stopping distance  $\lambda_p = VMb$ , where  $M$  is the mass of the particle. The smaller particles tend to reach the walls of a narrow channel by diffusion according to the deposition parameter  $D(L/Q)$ , where  $L$  is the length of the channel and  $Q$  is the volume flow rate of the carrier gas (Hinds, 1982). In the human respiratory tract, for instance, the large particles with a high  $M$  are deposited by impaction in the upper part, whereas the small nanoparticles penetrate to the alveoles of the lung were they reach the walls by diffusion.

**2.2. Surface area from the mass transfer coefficient.** The transfer of molecules of density  $n$  from the carrier gas to the nanoparticles of density  $N$  describes the growth of the nanoparticles by condensation of gas phase species. If every molecule that hits the particle also sticks to it, the rate of condensation is given by  $dn/dt = -KNn$  where  $K$  is the mass transfer coefficient. Obviously the sticking probability is usually  $< 1$ . For instance,  $\text{NO}_2$  or  $\text{O}_3$  have sticking probabilities on carbon nanoparticles of  $10^{-4}$  according to Kalberer et al. (1996) and Fendel et al. (1995). However, electrically charged molecules are reported to transfer at least their charge to any nanoparticle once they contact it. Reactive species such as metal atoms will also bind to any surface. This can be used to measure the mass transfer coefficient  $K$ . In the first method, ions are produced in the carrier gas and the electrical charge transferred to the nanoparticles is measured. In the second method, that may be applied even with very low densities of nanoparticles, the carrier gas

is doped with radioactive lead atoms produced in the decay of the noble gas atom radon. The radioactivity acquired by the nanoparticles provides a measure of  $K$  (Gäggeler et al., 1989). With a sticking probability of 1,  $dn/dt = dN^+/dt$ , where  $N^+$  is the density of electrically charged particles or radioactive particles depending on the experiment. This yields

$$(2) \quad N^+ = N_0[1 - \exp(-Ktn_0)]$$

where  $t$  is the time of interaction.  $n_0$  and  $N_0$  are the densities of the molecules or atoms and particles at  $t = 0$ .  $K$  has been determined according to Eq. (2) by letting the gas carrying the particles interact for a time  $t$  with the ions or the radioactive lead atoms, and observing the density  $N^+$  of charged or radioactive particles.

The theory of  $K$  depends again on the Knudsen number  $Kn$ . For  $Kn \gg 1$ , the gas molecules fly *in vacuo* near the particle. The rate with which they hit the particle depends on the averaged particle cross section and the average velocity  $v$  of the molecules. This yields

$$(3) \quad K = \frac{\pi}{4}vd_p^2.$$

For  $Kn \ll 1$ , the continuum theory applies and the molecules with diffusion constant  $\Delta$  diffuse to the particles. This yields  $K = 2\pi\Delta d_p$ . Hence, just like the friction coefficient  $1/b$ ,  $K$  scales with  $d_p^2$  in the molecular regime and with  $d_p$  in the macroscopic regime.

At  $Kn \simeq 1$ , the adsorbing species first have to perform a classical diffusion to the neighborhood of the particle where the gas kinetics dominate. Some authors have estimated the distance at which this transition occurs, but it turns out, as demonstrated by Filippov (1993), that the last step is best treated in a Monte Carlo calculation of the actual pathways of the molecules. This has the advantage over the older approximations that gas molecule collisions close to the particle are properly taken into account and that even complex interactions such as those occurring between a



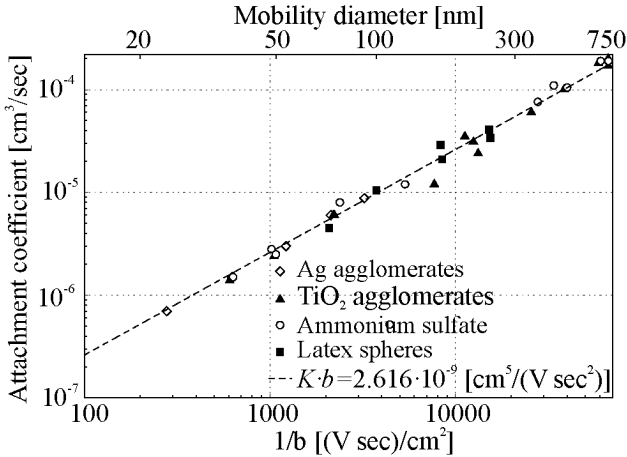


FIGURE 1.2. Mass transfer coefficient  $K$  plotted against the friction coefficient  $1/b$ . the mobility diameter  $d_p$  as calculated from  $b$  is also indicated. The data are adapted from Rogak et al. (1991) and Schmidt-Ott et al. (1990).  $K$  is determined by attachment of radioactive lead atoms. The carrier gas is air.

charged molecule and the image charge induced in the particle can be accounted for in a realistic way. At any rate, again a smooth transition occurs from the macroscopic regime where  $K \propto d_p$  to the molecular regime with  $K \propto d_p^2$ . If it were not for the necessity to assume a sticking probability of 1 in the measurement of  $K$ , and a constant mode of reflection of the gas molecules in the case of the mobility  $b$ , one might predict from inspecting the theory that at least near the molecular regime, both physically very different experiments depend on the active surface. This implies that a scaling law  $Kb = \text{const}$  should be valid independently of the particle size. This scaling law must be independent of the actual shape as well as of the chemical nature of the particle.

Rogak et al. (1991) and Schmidt-Ott et al. (1990) measured the mobility  $b$  of silver agglomerates, titanium oxide particles and their agglomerates, latex spheres, and ammonium sulphate droplets over a wide range of particle sizes and shapes. Simultaneously, the mass transfer coefficient was also determined using the radioactive lead method. Figure 1.2 shows the results of this experiment.  $K$  is plotted against the friction coefficient  $1/b$ . The mobility diameter  $d_p$  is calculated from  $b$  according to Fuchs (1964). The data extend well over the transition from the macroscopic to the molecular regime, and there is indeed no systematic difference between agglomerates with bizarre shapes and perfectly spherical particles. There is also no difference between metals such as Ag and perfect insulators such as latex spheres which means that the image charge potential is not important. The constant value of  $Kb = 2.616 \times 10^{-9} \text{ (cm}^5/\text{V s}^2\text{)}$  provides a fit to the data. Although there are fluctuations of up to 50% in a single measurement, a systematic deviation for one specific type of particle does not occur. This proves that the active surface determines both  $K$  and  $b$ , and that both physically very different experiments really measure the same particle property.

Figure 1.3 shows the results of our own experiments with a large variety of materials ranging from metals to insulators, and from perfect spheres to agglomerates and needle shaped single crystals of the amino acid L-tyrosine. The mass transfer coefficient was determined with the positive air ions produced in a glow discharge. Prior to admitting the carrier gas with the nanoparticles to the region containing the ions, any previously charged nanoparticles were removed by an electrofilter. Again,  $Kb = \text{const}$  is verified within experimental uncertainty, and no specific trend can be seen depending on the chemistry or the geometry of the nanoparticles in the range  $20 \ll d_p \ll 180 \text{ nm}$ . This suggests that the scaling law  $Kb = \text{const}$  is universal and also that the concept of the active surface makes sense.

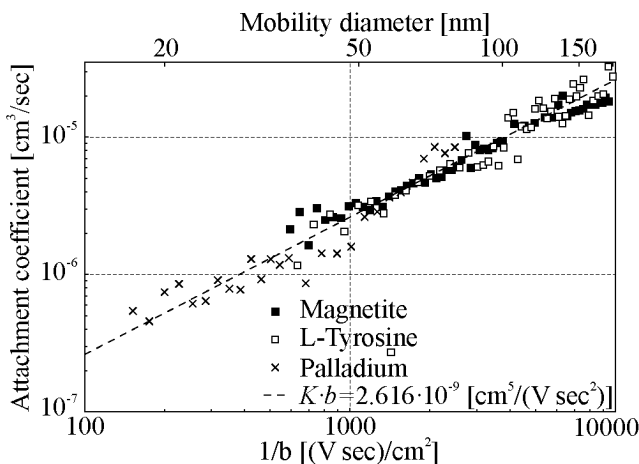


FIGURE 1.3. Mass transfer coefficient  $K$  vs the friction coefficient  $1/b$  for Pd,  $Fe_3O_4$ , and L-Tyrosine particles. The mobility diameter  $d_p$  is also indicated.  $K$  is determined by attachment of positive air ions to neutral particles. The carrier gas is air.

### 3. Chemical fingerprint of the active surface

The yield  $Y$  of photoelectrons with photon energies near photoelectric threshold delivers a fingerprint of the physical and chemical state of the surface of condensed matter, and depends on optical absorption, that is on bulk properties as well. The advantage of this oldest form of photoelectron spectroscopy is that one can make use of powerful and innovative sources of light such as excimer lamps and pulsed lasers opening up investigations in the time domain as well. The main disadvantage is that threshold photoemission is still poorly understood and in many cases can be interpreted on a phenomenological basis only.

If the sample is immersed in a gas instead of vacuum, the photoelectrons collide with gas molecules, perform a random motion near the sample surface, and eventually diffuse back to it. Therefore, no steady-state photoelectric conductivity

is observed with macroscopic samples unless one applies an electric field. However, if the dimensions  $d_p$  of a particle are small compared to the mean free path  $\lambda_e$  of electrons in the gas, then backdiffusion of the photoelectrons is unlikely. This occurs with gases at normal conditions for  $d_p$  in the nanometer size range. It has been detected by observing photoconductivity with Ag nanoparticles in air (Schmidt-Ott et al., 1980). The condition for this experiment is that the photon energy is below the photoionization energy of the carrier gas, but above the photoelectric threshold of the particles. In the actual practice the photoelectrons are removed by applying an alternating electric field or by letting them diffuse to the walls, and the positive charge left behind on the particles is measured by guiding the gas carrying the particles through a filter in which the particles are precipitated. The electric current flowing to the filter yields the total electric charge carried by the particles.

This simple experiment revealed that some nanoparticles exhibit an extremely large photoelectric yield  $Y$  which depends strongly on small amounts of adsorbates. The enhancement of  $Y$  with Cu, Ag, Au, Pd, and Ni particles of  $d_p = 3$  nm in purest He turns out to be 100-fold compared to macroscopic surfaces (Schleicher et al., 1993). At the photon energy  $h\nu = 10$  eV,  $Y$  approaches unity with Ag particles in He, that is every incident photon produces almost one photoelectron while the spectral dependence of the yield remains essentially identical to the one observed on bulk Ag (Chüller et al., 1988). Another remarkable observation is that urban air contains particles with  $d_p = 100$  nm with a photoelectric threshold below 5 eV. These particles do not disappear in fog or rain (Burtcher and Siegmann, 1994) which means that water does not condense on them. It turned out that polycyclic aromatic hydrocarbons (PAH) adsorbed at the particle surface are generating the high photoelectric yield of these particles, in fact, it is possible to determine the density of adsorbed PAH in ambient air by measuring  $Y$  (Burtcher, 1992). PAH are an issue in public health protection as some species are potent carcinogens, and one knows that they induce lung cancer in humans. The most prominent sources in urban air are

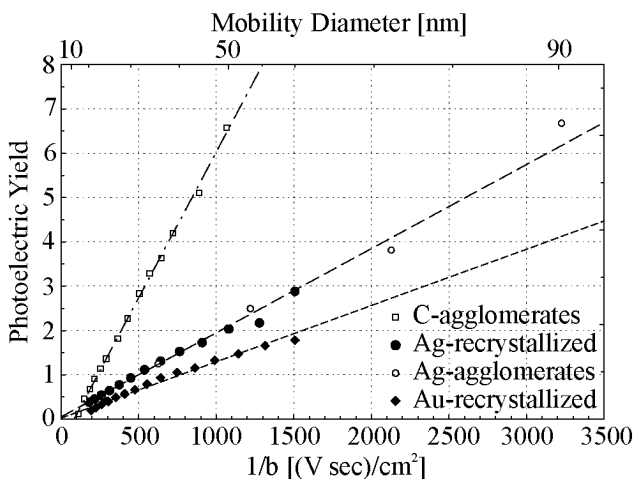


FIGURE 1.4. The photoelectric yield  $Y$  in arbitrary units vs the friction coefficient  $1/b$  for various particles. The data for Ag agglomerates, and C agglomerates are from Schmidt-Ott et al. (1990) and Burtscher (1992) respectively, and the recrystallized Ag and Au agglomerates are our own measurements. The mobility diameter is also given.

diesel vehicles, but every incomplete combustion, be it wood or coal fire, or cigarette smoke contributes particles with PAH adsorbed at the surface. Hence particles with high  $Y$  in ambient air invariably point to a nearby combustion source.

To do proper surface science with nanoparticles, one has to separate the effects on the photoelectric yield stemming from physical properties such as particle size and surface roughness from the ones induced by the chemical composition of the bulk and at the surface. The window of photon energies useable in photoelectric charging of nanoparticles is narrow;  $h\nu$  must be lower than the photoionization energy of the carrier gas but above the work function  $\phi$  of the nanoparticles. In air, one additionally might have to stay below the photon energy inducing excessive ozone

formation. Under this condition,  $h\nu \geq \phi$ , photoelectrons with quite low kinetic energy may be emitted from the surface of the particles into the carrier gas. However, the photoelectron must not be reabsorbed by the particle. It is immediately clear that the inner surfaces will not contribute to photoelectric emission. But the emission from cracks and incisions is not as large as calculated from the geometrical area of the surface because there is a high probability that the emerging photoelectron hits some other part of its parent particle surface and gets reabsorbed. Therefore, it is not surprising that the surface area accounting for the emission of charges from the particle equals the one responsible for the absorption of ions at least in the molecular regime where the ions fly on straight trajectories to the particle. Figure 1.4 shows measurements of the photoelectric yield  $Y$  plotted against the friction coefficient  $1/b$  which is the active surface. The data are for carbon agglomerates (Burtscher, 1992), silver agglomerates (Schmidt-Ott et al., 1990), gold agglomerates, and recrystallized Ag and Au agglomerates. We see that indeed there is a linear relationship between  $1/b$  and  $Y$ , but the constant of proportionality does depend on the material and on the photon energy, hence, contains the desired chemical fingerprint of the nanoparticle. The physical parameters of particle shape and size can thus be eliminated by a measurement of the mobility  $b$  or equivalently a measurement of the mass transfer coefficient  $K$ . This is extremely helpful considering the bizarre shapes of the agglomerates shown in Figure 1.1. One then has a new scaling law  $Yb = \text{const}$  or equivalently  $Y/K = \text{const}$ . These laws are important as they show that the chemical fingerprint of the particles may be obtained even with a distribution of particle sizes  $N(d_p)$ , and without knowledge of the number density. The total photoelectric charge PC carried by the ensemble of particles is

$$(4) \quad \text{PC} \propto \int_0^{\infty} YN dd_p,$$

while the total charge by ion attachment IC is

$$(5) \quad \text{IC} \propto \int_0^{\infty} KN dd_p.$$

Equation (5) follows from Eq. (2) if the product of ion density  $n_0$  and the time  $t$  spent in the ion charger is chosen to be low so that  $\exp(-Ktn_0) \simeq 1 - Ktn_0$ . With  $Y \propto 1/b$  and  $K \propto 1/b$  one obtains

$$(6) \quad \frac{\text{PC}}{\text{IC}} = \text{CF}.$$

CF is a constant that depends only on the photon energy used in PC and on the chemistry of bulk and surface of the particles, hence, it delivers “on-line” the desired chemical fingerprint of the ensemble of particles  $N(d_p)$  without doing any size analysis and without counting the particles. This has been applied for instance to distinguish particles of different origin in automotive exhaust, namely the carbonaceous particles formed in incomplete combustion of the gasoline from the mineralic particles formed out of fuel additives (Matter et al., 1999). This is of importance, as the reduction of carbonaceous particle emission is the responsibility of the engine manufacturer, while the particles from contaminants of the fuel are in the responsibility of the gasoline producers. Furthermore, even carbonaceous particles from different types of combustion can be distinguished. This is helpful as particles from different combustions carry a different blend of chemicals and therefore pose a different health risk. It turns out, for instance, that a flickering candle produces particles with high CF, while cigarette smoke exhibits an almost ten times lower CF (Siegmann et al., 1999). Fresh diesel particles are identified readily by their specific CF which is the same all over the world. Diesel particles are the most prominent part of particulate air pollution in major cities like Tokyo and Paris (Zhiqiang et al., 2000). It is obvious that such techniques, amongst many other applications, will provide a basis for quantifying the health risk imposed by particulate air pollution.

As an example for the observation of the dynamics of the active surface we discuss the measurement of perylene  $\text{C}_{20}\text{H}_{12}$  desorption from graphite particles (Hueglin et al., 1997). An excimer laser delivers pulses of photons of 6.42 eV energy, the pulse length is 20 ns. The flat perylene molecule containing five aromatic

rings was chosen because it stands as a typical representative of the PAH formed in combustion. The well-known carcinogen Benzo(a)pyrene is built with five aromatic rings as well and should therefore exhibit very similar adsorption/desorption kinetics. In this experiment, the carbon particles are produced in a carrier gas at ambient temperature in which a partial pressure of perylene is maintained. The perylene adsorbs on the particles until an equilibrium between adsorption and desorption is reached corresponding to the density of perylene molecules  $n_{\text{CH}}$  in the carrier gas and to the number of adsorption sites on the particle. Subsequently a small volume of the gas carrying the perylene loaded particles is transported into the hot carrier gas with  $n_{\text{CH}} = 0$  at the temperature  $T > T_0$ . Now perylene will start to desorb from the particles. The desorption of perylene induces a decrease of the photoelectric yield. After a preset time, the UV laser is fired, and the time dependence of the decrease of  $Y$  can be observed by measuring the photoelectric charge on the particles. Figure 1.5 shows the time dependence of the desorption for two temperatures of the carrier gas. From these measurements, one obtains the adsorption enthalpy of perylene on the particle. The experiment is analog to thermal desorption studies *in vacuo*, one of the most fruitful techniques in surface science.

Besides source attribution of combustion aerosols (Siegmann et al., 1999; Zhiqiang et al., 2000) and disclosing their surface dynamics as demonstrated in Figure 1.5, photoelectric charging of nanoparticles has also been used to study catalytic reaction on soot particles (Kasper et al., 1999b). Furthermore, circular dichroism in the photoionization of nanoparticles built with chiral molecules has also been detected (Paul and Siegmann, 1999). This makes it possible to distinguish nanoparticles of biological origin from particles synthesized in nonchiral chemical reactions.

#### 4. Theoretical background of the scaling laws

Scaling laws are important in physics as they allow one to generalize the complex phenomena observed for instance in phase transitions. Schmidt-Ott et al. (1990)



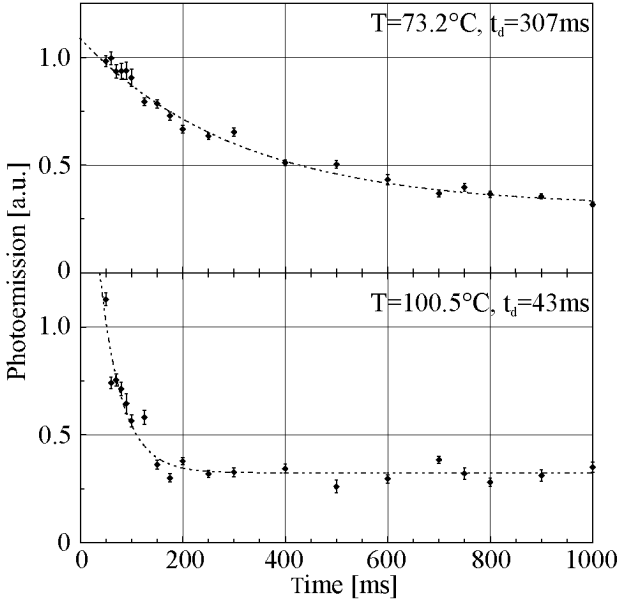


FIGURE 1.5. Desorption of perylene from carbon agglomerates of mobility diameter  $d_p = 25$  nm at  $T = 72.3^\circ\text{C}$  and  $T = 100.5^\circ\text{C}$ . The dotted lines are exponentials with the time constants  $t_d = 307$  ms and  $t_d = 43$  ms respectively, from Hueglin et al. (1997).

have described scaling laws for mass, surface, and mobility radius of fractal-like agglomerated particles; the term “exposed” surface is used in this work instead of active surface employed here. We have given experimental evidence that the following more restricted scaling laws are universal extending to spherical nanoparticles and restructured agglomerates as well. These general scaling laws on changing the particle size are:  $Kb = \text{const}$ ,  $Yb = \text{const}$ , and  $KD = \text{const}$ , where  $b$  is the mobility,  $Y$  is the photoelectric yield for threshold photoelectrons,  $D$  is the diffusion constant of the particles, and  $K$  is the mass transfer coefficient. We have shown that  $K$  may

also be determined by simply measuring the electrical charge acquired by neutral particles on adding ions to the carrier gas. We will now discuss some theoretical implications.

The fact that the scaling law  $Kb = \text{const}$  is independent on whether the particle is a metal or an insulator demonstrates that the role played by the image force in the approach of an ion is negligible. For conducting particles the image charge potential is largest. The potential energy of ions in an induced image field of a spherical metallic particle with radius  $a$  is

$$(7) \quad U = \frac{1}{4\pi\epsilon_0} \frac{e^2 a^3}{2r^2(r^2 - a^2)},$$

where  $e$  is the elementary charge and  $r$  the distance from the particle center. The image charge increases the probability of charging by bending the trajectories of passing ions towards the particle. This is estimated to be significant if  $U$  becomes comparable to the average ion kinetic energy  $E_k = 3/2kT$  at distances from the particle surface of the order of the particle radius. For example, equating  $U$  and  $E_k$  at  $r^2 = 2a^2$  one obtains an estimate for the critical particle size below which the image charge potential should become important

$$(8) \quad a_{\text{cr}} = \frac{1}{4\pi\epsilon_0} \frac{e^2}{6kT}.$$

This yields  $d_p = 2a_{\text{cr}} \simeq 20$  nm. The present measurements displayed in Figure 1.3 extend only to  $d_p \geq 20$  nm. At lower mobility diameters, one should observe an increase in  $Kb$  depending on  $\epsilon(\omega)$ , the frequency dependent dielectric constant of the particle. This increase, if it can be observed, might provide a new test of the electronic properties of mesoscopic matter. Such information is urgently needed in cluster science, for instance to better understand the elusive nature of cloud condensation nuclei (Kulmala, 1999).

Due to the absence of a theory for the mobility  $b$  in the transition between molecular and hydrodynamic motion of the particle, there is no rigorous proof for

$Kb = \text{const.}$  However, formulae that are tested empirically exist for both  $K$  and  $b$  (Williams and Loyalka, 1991; Fuchs, 1964). Sherman (1963) found that existing experimental data can be adequately described by the empirical formula

$$(9) \quad \frac{q}{q_c} = \frac{1}{1 + q_c/q_f},$$

where  $q$ ,  $q_c$ , and  $q_f$  are the transfer rates in the transition, continuum, and free-molecular regime, respectively. Correspondingly, for the mass transfer coefficient we have (Williams and Loyalka, 1991)

$$(10) \quad \frac{K}{K_c} = \frac{1}{1 + \sqrt{\pi}Kn},$$

where  $K_c$  is the continuum-regime mass transfer coefficient.

Similarly, using the Cunningham correction factor (Williams and Loyalka, 1991) for the particle mobility we obtain

$$(11) \quad \frac{b}{b_c} = 1 + Kn [A_1 + A_2 \exp(-A_3/Kn)],$$

where  $b_c$  is the particle mobility in the continuum limit and the values of the constants can be taken as  $A_1 = 1.257$ ,  $A_2 = 0.4$  and  $A_3 = 1.1$ . The last two equations yield

$$(12) \quad Kb = K_c b_c \frac{1 + Kn [A_1 + A_2 \exp(-A_3/Kn)]}{1 + \pi^{1/2}}.$$

This equation predicts that the product  $Kb$  can vary only slightly, within 14%, as  $Kn$  increases from 0 to infinity. The deviations are largest for  $Kn = 1$ . This region should be tested carefully to find out whether this deviation is real or an artifact of the interpolation schemes. It also might be possible that with an inert carrier gas and nonpassivated surfaces, the scaling breaks down due to different reflection modes of the carrier gas molecules at the particle surface. Plotting  $Kb$  is the most obvious way to detect such an effect if it exists.

The scaling laws containing the photoelectric yield  $Y$ , namely  $Yb = \text{const.}$ ,  $Y/K = \text{const.}$  and  $YD = \text{const.}$  so far have only been tested for particles with

$d_p < 100$  nm. For larger particles with  $d_p > 200$  nm, the onset of classical diffusion leads to backdiffusion of the photoelectric charges to the particle. According to Filippov et al. (1993), the probability  $p_e$  of liberation of a photoelectric charge is given by

$$(13) \quad p_e = 1 + \frac{3}{4Kn_e}^{-1}.$$

$Kn_e = \lambda_e/d_p$  is the Knudsen number for the free electrons with  $\lambda_e$  the mean free path of low energy electrons in the carrier gas. In air it takes many collisions before the free electron attaches itself to  $O_2$  and produces the negative ion  $O_2^-$ . In  $N_2$  gas, no negative ions are formed and  $\lambda_e = 670$  nm at normal conditions. It is assumed that this value for  $\lambda_e$  also applies to air. Equation (8) yields then  $p_e \simeq 0.5$  for  $d_p = 500$  nm, while  $p_e = 1$  for  $Kn_e \gg 1$  (small particles) and  $p_e = 0$  for  $Kn_e \ll 1$  (large particles in the micrometer range). The photoelectric yield of a particle is given by  $Y = (\pi/4)d_p^2yp_e$  where  $y$  is the yield per unit area of the active surface. The effective specific yield  $yp_e$  decreases as the particle increases but at a different rate compared to the active surface responsible for the friction coefficient  $1/b$ . It is therefore not expected that the scaling laws containing  $Y$  are valid for larger particles approaching the micrometer range. Yet this still waits detailed experimental and theoretical investigation.

## 5. Conclusions

Surface characteristics of mesoscopic condensed matter or nanoparticles can be evaluated while the particles are suspended in a carrier gas. There are three physically very different experiments to determine the area of the active surface, namely the measurement of the mass transfer or attachment coefficient  $K$ , the mobility  $b$ , and the diffusion constant  $D$ . Combining one of these experiments, preferably the attachment of positive gas ions to the particles with photoelectric charging makes it

possible to obtain a chemical fingerprint of the particles without knowing their number or their sizes. It amounts to separating the effects of the physical shape and size of the sometimes bizarre agglomerates from their chemistry. This arises because ion attachment determines the total area of the active surface of the ensemble of particles while photoelectric emission of low energy electrons is also proportional to the same active surface but additionally contains a factor depending on the chemical nature of the particles. By choosing the appropriate light source, one can be highly sensitive to a specific adsorbate/particle system. Using pulsed lasers, it will be possible to observe the surface dynamics down to the femtosecond time scale.

The empirical scaling laws  $Kb = \text{const}$ ,  $Yb = \text{const}$ ,  $YD = \text{const}$  and  $Y/K = \text{const}$  connect different phenomena such as particle friction, surface growth by condensation of gas phase species, particle diffusion to a wall, attachment of gas ions, and the photoelectric yield  $Y$ . The scaling laws are extremely helpful for comparison and calibration of instruments based on very different physical principles. Possible deviations from the scaling laws might turn out to yield additional information on the particles, for instance concerning their dielectric properties, or the mode of reflection of the carrier gas molecules on the surface.

The scaling laws point to the importance of the active surface which has also been termed Fuchs surface (Gäggeler et al., 1989) and exposed surface (Schmidt-Ott et al., 1990). The active surface determines the rate of particle growth by surface condensation, the ultimate speed of chemical reactions involving the carrier gas, and the catalytic activity. The active surface also determines the deposition of particles by impaction and by diffusion in particle filters. For example, knowing the active surface one can predict particle deposition in the inner and outer human respiratory tract. Therefore, the active surface is one of the most important physical properties of nanoparticles in a carrier gas and should be chosen in the future to characterize nanoparticle air pollution. Surface science with nanoparticles in a carrier gas is

a young field with excellent chances for further growth and numerous important applications.

## **Effects of second order processes in aerosol monitoring**

ABSTRACT. We present a general-purpose mathematical model for pollution concentration studies. The model is an approximate solution for the time dependence of size distribution that takes into account processes like aerosol coagulation and condensation among others. Our model is validated by representative experiments using standard aerosol monitoring devices that measure light scattering, particle cross section, particle bound polycyclic aromatic hydrocarbons (PPAH) and number concentration, showing an excellent agreement with the experimental data. The results demonstrate that aerosol coagulation has to be taken into account when monitoring aerosol particles. We also show that the simultaneous application of different sensors reveals new information about the physical and chemical properties of the aerosol.

---

\*Published in: A. Keller, and K. Siegmann, *J. Aerosol Sci.* 32(11):1235-1247, 2001; A. Keller and H.C. Siegmann, *J. Exposure Anal. Environ. Epidemiol.* in print.

## 1. Introduction

It has been shown that a mass balance model used in combination with portable aerosol sensors is suitable for estimations of indoor particulate concentrations and cigarette emission rates (Ott et al., 1992; Klepeis et al., 1996; Brauer et al., 2000). More specific, such a method has been used to estimate the indoor particle-bound polycyclic aromatic hydrocarbons (PPAH) concentration coming from traffic (Dubowsky et al., 1999), environmental tobacco smoke (Ott et al., 1994) and other indoor combustion sources (Ott and Klepeis, 1995). Yet, the method of these studies is designed to be used when measuring aerosol mass with a piezoelectric balance or when monitoring ambient gas concentration and therefore it just accounts for the indoor-outdoor exchange rate, particle deposition rate and other properties which involve first order processes in a mass balance differential equation. Nevertheless, when using sensors that measure properties other than aerosol mass, as is the case of number concentration, cross section, photoionization, or light scattering, or when measuring aerosol mass indirectly (i.e. when using most portable-sensors) second order processes, such as aerosol coagulation, must be considered.

In this chapter we derive a model based on the general dynamic equation (GDE) for aerosol samples that exhibit a narrow size distribution. The model is valid for studies of number concentration, particle cross section, volume, total light scattering, and other properties which can be expressed in terms of moments of the size distribution. A comparison between the model derived from the GDE and mass balance model will also be presented. The model will be validated with our experimental data obtained from aerosol devices that work on different principles and as an application example the total PPAH emission of a cigarette will be calculated. It will also be shown that the comparison of different sensors reveals more information on physical and chemical properties of the aerosol.



## 2. Theory

**2.1. General Dynamic Equation.** The particle size distribution of a polydisperse aerosol is described by the general dynamic equation (GDE) (Friedlander, 2000). In the case of a well mixed room of volume  $V$  with air flow rate  $\omega$ , and an indoor source producing aerosol at a rate  $g$ , the GDE can be written as

$$(14) \quad \begin{aligned} \frac{dn(v, t)}{dt} = & - \frac{\partial\{I(v) \cdot n(v, t)\}}{\partial v} + \frac{1}{2} \int_0^v \beta(v - \bar{v}, \bar{v})n(v - \bar{v}, t)n(\bar{v}, t)d\bar{v} \\ & - n(v, t) \int_0^\infty \beta(v, \bar{v})n(\bar{v}, t)d\bar{v} - \frac{d(v)}{V}n(v, t) + \frac{g(v, t)}{V} \\ & + \frac{\omega}{V} [x_0(v, t) - n(v, t)], \end{aligned}$$

where  $n(v, t)$  is the particles size distribution at a time  $t$ ,  $v$  is the particle volume,  $I(v)$  is the single-particle growth rate by condensation,  $\beta(v, \bar{v})$  is the collision kernel,  $d(v)$  is the rate of particle loss due to diffusion to the walls, and  $x_0(v, t)$  is the outdoor aerosol concentration.

Now, let us look at the physical interpretation of some important moments of the size distribution. The  $k$ th moment of the size distribution function  $n(v, t)$  is defined as

$$(15) \quad M_k(t) = \int_0^\infty v^k n(v, t) dv,$$

where  $k$  is an arbitrary real number. The zeroth moment,

$$(16) \quad M_0(t) = \int_0^\infty n(v, t) dv = N(t)$$

is the total concentration of particles and the first moment is the total volume of the particles per unit volume of gas:

$$(17) \quad M_1(t) = \int_0^\infty vn(v, t) dv = \phi(t)$$

where  $\phi$  is the volume fraction material in the fluid.

Other physical properties can be expressed by different moments. Since for very small particles the light scattering follows the Rayleigh model, the intensity

of the scattered light is proportional to  $d_p^6$  and the total Rayleigh scattering can be written as

$$(18) \quad b_{\text{scat}} \propto M_2 \quad (\text{small particles}).$$

On the other extreme, the scattering intensity in the optical range corresponds to  $I \propto d_p^2$ , and its total intensity can be written as

$$(19) \quad b_{\text{scat}} \propto M_{2/3} \quad (\text{large particles}).$$

Similarly, if we assume that the surface of a particle is  $S \propto d_p^2$  and its volume  $v \propto d_p^3$ , then the total aerosol surface per unit volume gas  $A$  is given by

$$(20) \quad A \propto M_{2/3}.$$

Therefore, a population balance equation written in terms of the GDE for different moments  $M_k$  can be used to study the changes in number concentration ( $k = 0$ ), particle cross section ( $k = 2/3$ ), mass and volume ( $k = 1$ ), and light scattering ( $2/3 \leq k \leq 2$ ), among others. Additionally, such an equation can even be used in the case of aerosols composed of agglomerates with fractal dimension  $D_f$  by taking into account the power law relationship  $v \propto d_p^{D_f}$ .

**2.2. Population balance equation.** By multiplying equation (14) by  $v^k$  and integrating over  $v$  we obtain the change in moment:

$$(21) \quad \begin{aligned} \frac{\partial}{\partial t}(M_k) = & k \int_0^\infty v^{k-1} I(v) n(v, t) dv - \frac{1}{V} \int_0^\infty v^k [d(v) + \omega] n(v, t) dv \\ & + \frac{1}{2} \int_0^\infty \int_0^\infty [(v + \bar{v})^k - v^k - \bar{v}^k] \beta(v, \bar{v}) n(v, t) n(\bar{v}, t) dv d\bar{v} \\ & + \frac{1}{V} \int_0^\infty v^k g(v, t) dv + \frac{1}{V} \int_0^\infty v^k x_0(v, t) dv, \end{aligned}$$

Equation (21) describes the population balance for the different moments. It is highly non-linear but it may be rewritten in a simplified form assuming a nearly monodisperse system. For an aerosol with narrow size distribution and average volume  $v$  we

can write  $M_k = v^k N(t)$ , where  $N(t)$  is the total number of aerosol particles. Thus, equation (21) becomes

$$(22) \quad \frac{\partial}{\partial t}(M_k) = \frac{\omega}{V}[x_{0,k}(t) - M_k] + \frac{g_k(t)}{V} - \frac{d}{V} - \frac{kI}{v} M_k - \frac{1 - 2^{k-1}}{v^k} K M_k^2,$$

where  $g_k(t) = v^k g(t, v)$  and  $x_{0,k}(t) = v^k x_0(v, t)$  are the contributions from the indoor-source and outdoor-concentration to the  $k$ th moment and  $K$  is the coagulation coefficient.

We can notice immediately the similarity between equation (22) and the mass balance equation. The first term on the right hand side of the equation is the change in the  $k$ th moment due to air exchange, the second is the indoor source contribution, and the third is the change in moment due to sinks (diffusion losses) and sources (condensation or particle nucleation) inside the chamber. We also notice that the coagulation contributes as a quadratic term for the moments  $k \neq 1$ . This would yield an error if we try to describe properties other than mass and volume by using the mass balance model.

Now, let us define the first order moment change rate as

$$(23) \quad \beta_k \equiv \frac{d}{V} - \frac{kI}{v}$$

and the second order change rate as

$$(24) \quad K_k \equiv \frac{2 - 2^k}{v^k} K.$$

Thus, equation (22) becomes

$$(25) \quad \frac{\partial}{\partial t}(M_k) = \frac{\omega}{V}[x_{0,k}(t) - M_k] + \frac{g_k(t)}{V} - \beta_k M_k - \frac{1}{2} K_k M_k^2,$$

In the case of the zeroth moment (number concentration)  $K_0 = K$  is the actual coagulation coefficient and  $\beta_0 = d/V$  is reduced to the particle loss by diffusion since condensation has no influence in number concentration. For  $k = 1$ ,  $M_1$  represents total mass or volume, and  $K_1 = 0$ . Finally, for moments  $M_{k>1}$ , as in the case of

Rayleigh scattering ( $k = 2$ ), the coagulation would have a positive contribution to the total moment since  $K_k < 0$ .

If, for simplicity, we assume a constant outdoor concentration  $x_{0,k}(t) = x_{0,k}$  and an indoor source with constant strength over time  $g_k(t) = g_k$  we can solve eqn. (25) as

$$(26) \quad M_k(t) = \frac{\Gamma + \beta_k + \frac{\omega}{V} e^{-\Gamma(t-t_1)} + \Gamma - (\beta_k + \frac{\omega}{V}) \frac{K_k M_k(t_1) + \Gamma + \beta_k + \frac{\omega}{V}}{K_k M_k(t_1) - \Gamma + \beta_k + \frac{\omega}{V}}}{K_k \left[ \frac{K_k M_k(t_1) + \Gamma + \beta_k + \frac{\omega}{V}}{K_k M_k(t_1) - \Gamma + \beta_k + \frac{\omega}{V}} - e^{-\Gamma(t-t_1)} \right]},$$

which is the indoor aerosol concentration at a given time  $t > t_1$ ,  $M_k(t_1)$  denotes the value of the  $k$ th moment at time  $t_1$ , and

$$(27) \quad \Gamma \equiv (\beta_k + \omega/V)^2 + 2K_k(g_k + \omega x_{0,k})/V^{1/2}.$$

We shall now analyze some specific cases of equation (26) and validate it against the first order mass balance model. Lets assume that the outdoor concentration  $x_{0,k} = 0$ , which is valid for a controlled experiment in an isolated indoor space. Simplifying, we can add together the first coefficients and write them as  $\Phi = \beta_k + \omega/V$  (also known as the effective air exchange rate). We can distinguish now between two cases: a production process with a source emitting aerosol at a constant rate  $g_k$  for a time interval  $t_1 \leq t \leq t_2$ , and a decay process where  $g_k = 0$  for a time  $t > t_2$ .

During the emission event  $t_1 \leq t \leq t_2$  and  $\Gamma = \Phi^2 + 2K_k g_k / V^{1/2}$ . At this point, we can compare our result with the linear model by setting the value of  $K_k = 0$ , obtaining

$$(28) \quad M_{k,\text{lin}}(t_1 \leq t \leq t_2) = \frac{g_k}{V\Phi} \left[ 1 - e^{-\Phi(t-t_1)} \right] + M_k(t_1) e^{-\Phi(t-t_1)},$$

which is the expected simple exponential expression for the mass balance model (Ott et al., 1992).

For the decay process  $t > t_2$ ,  $g_k = 0$ ,  $A = \Phi$ , and eq. (26) becomes

$$(29) \quad M_k(t > t_2) = \frac{K_k}{2\Phi} + \frac{1}{M_k(t_2)} e^{\Phi(t-t_2)} - \frac{K_k}{2\Phi}^{-1}.$$

Equation (29) has a simpler form than our general solution (equation (26)), and describes the concentration decay in the case when no indoor sources are present.

Here again by making the quadratic term coefficient  $K_k = 0$ , we obtain the simple exponential decay that involves a linear model

$$(30) \quad M_{k,\text{lin}}(t > t_2) = M_k(t_2)e^{-\Phi(t-t_2)}.$$

Note that by using a sink coefficient  $K_k \neq 0$  the decay would yield a different result than in the case of the simple exponential. This is especially important for our example of source strength determination, where we analyze the decay and calculate the values for  $\Phi$  and  $K_k$  to estimate the concentration in the room at the time when the source was extinguished. It also plays an important role when measuring in places where the air is not mixed fast because we would have to wait for the moment when a stable condition is reached.

### 3. Methods

We performed a series of indoor experiments to monitor several particle properties from aerosol coming from sidestream cigarette smoke. The experimental setup was based on the one suggested for chamber measurements by Ott et al. (1992) and Brauer et al. (2000). Four cigarettes were set alight simultaneously by a smoking machine (Filtrona, model 302) and left to burn by themselves (smolder smoked). After burning, they were put out by dousing them into water. The experiments were done inside a  $77 \text{ m}^3$  room with two ventilators placed inside it to ensure a fast mixing of the cigarette smoke. During and after the burning process, sensors based on different particle properties were acquiring data every 10 seconds. The flow rate of the sensors was chosen to be 1.5 l/min and their exhaust was filtered and released again into the room.

On another set of experiments, we sampled the aerosol in the mainstream smoke by setting the smoking machine to burn the cigarettes performing puffs every 60 s. The mainstream smoke was collected into filters and the filtered air was released into the room. The filters were then analyzed to determine the amount of PAH on them by means of a commercial Gas Chromatography Mass Spectroscopy (GCMS).

In both cases, the same commercially available filter cigarettes were used. On average each cigarette burned for about 8 minutes when smoked by the machine and 11 minutes when let to smolder.

**3.1. PPAH.** A portable PPAH sensor (EcoChem PAS 2000 CE) was used to measure the PPAH concentration during the experiments. The photoelectric aerosol sensor (PAS) uses an excimer lamp to expose the aerosol flow to UV radiation with an energy  $h\nu$  below the threshold for ionization of the gas molecules but above the photoelectric threshold of the particles (i.e. photoelectrons are emitted from the particle). The emitted photoelectric current is determined by collecting the positively charged particles on a filter and determining the current to ground potential. The wavelength of the excimer lamp is chosen in such a way that the photoelectric yield is mainly governed by the yield coming from aerosol particles which have PAH molecules adsorbed on their surface (Kasper et al., 1999a). The resulting photoelectric current establishes in fact a signal which is proportional to the mass concentration of PPAH (Burtscher and Siegmann, 1994).

**3.1.1. Calibration of PPAH sensors.** The Ecochem PAS 2000 CE sensors are sold with a calibration for traffic combustion aerosols. Since these sensors do not measure PAH mass directly, a new calibration has to be done when changing the aerosol source since aerosols coming from different sources tend to have a different PPAH composition. In our case, the calibration was done for particles emitted from the combustion of the test cigarettes.

In the same room used for the indoor measurements (a well ventilated and mixed  $77 \text{ m}^3$  room), the test cigarettes were burned using the smolder method. Four to six cigarettes were burned simultaneously (average burning time 11 min.) waiting between 30 and 60 minutes before the next set of cigarettes was burned in order to avoid a saturation of the sensor. A total of 70 cigarettes were burned in a 13 hours period. During this time the aerosol concentration was monitored by the PAS 2000 CE sensor. Additionally a filter was sampling the aerosol in the room at a flow rate of  $0.84 \text{ m}^3/\text{h}$  in order to do a GCMS and compare the sample amount of PAH with the integrated signal obtained from the PPAH sensor.

**3.2. Diffusion Charging.** An Ecochem DC 2000 CE diffusion charging sensor was also used in the indoor experiments. This sensor works by producing positive charged ions by a glow discharge formed in the neighborhood of a thin wire. The ions are repelled by the wire which is at positive potential and travel to the space containing the particles. During this, the ions have a probability of attaching to a particle. If this happens the particle carries the charge. The gas containing the particles is then sampled in a filter where the current flowing from the filter to ground potential is measured. For very small particles, the probability of one of the ions hitting the surface of the particle and sticking to it is proportional to the cross section of the particle. Hence, this instrument measures the active surface of small particles (Keller et al., 2001) without being sensitive to the chemistry (Qian et al., 2000).

**3.3. Light scattering.** We used a TSI Dusttrak (model 8520) which is a portable, battery operated instrument that measures the scattering of infrared light coming from a GaAs-laser-diode at an angle of  $90^\circ$ . It has an impactor at the sample entrance that removes all particles above  $10 \mu\text{m}$ , and gives a value of PM10 mass per  $\text{m}^3$ . The calibration of the instrument depends on the particle size distribution, and therefore on the particle source. It is factory set to relate the intensity of the scattered light to

the particle mass concentration of a standard aerosol sample (A1 test dust, previously know as “Arizona dust”) which exhibits a wide size distribution.

**3.4. Number Concentration.** To estimate the number concentration of aerosol particles, a continuous-flow Ultrafine Condensation Particle Counter (TSI CPC model 3025A) was used. The CPC is a device specially designed for detection of particles with a size smaller than the wavelength of visible light (down to 3 nm). Particles that enter the measurement device serve as condensation nuclei for oversaturated butanol vapor and grow. The butanol covered particles are then big enough to be counted individually by means of light scattering.

## 4. Results and Discussion

**4.1. Indoor measurements.** Figure 2.1 shows the aerosol concentration, produced by setting alight four cigarettes, as measured by the TSI Dusttrak, Ecochem DC 2000 CE, Ecochem PAS 2000 CE and TSI CPC 3025A. The cigarettes burned until the point where the concentration reaches a maximum and were then put out. We calculated the dashed lines by fitting the model to the decay part, using equation (29) and the Levenberg-Marquardt algorithm. The first part was then plotted taking the fitted values, the initial indoor concentration and the cigarette burn time as parameters to calculate the emission rate  $g_k$ . For this, the Newton method was employed. As can be seen in the figure, the model shows an excellent agreement with the experimental data.

A close examination of figure 2.1 reveals the presence of an upward curvature in the decay part of all the plots when using a semi-logarithmic scale. This points out that accounting for the second order terms is indeed important when using those devices. The effect of this curvature is highlighted in both, figure 2.2 and table 2.1, where a comparison with a fit to the first order model is shown. As can be seen from the calculated residual values (table 2.1), the curvature implies that by fitting the data to a model that includes only up to the first order coefficients we would



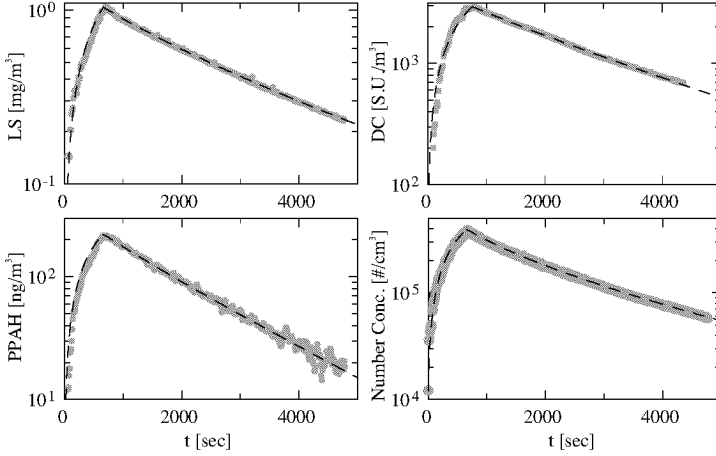


FIGURE 2.1. Semi-logarithmic plot of the aerosol concentration produced by simultaneously burning four cigarettes, as measured by a Dusttrak (Light Scattering, LS), DC 2000 CE (Diffusion Charging, DC, in surface units per  $\text{m}^3$ ), PAS 2000 CE (PPAH) and CPC 3025A (number concentration), compared to the concentration calculated by the model (dashed lines). The model was fitted to the decay part of the curves and the results were used to calculate the emission curve.

be underestimating the real values. This difference will even be higher for data projected outside the fitting interval (figure 2.2). A similar measurement for an inert gas or with a device that measures aerosol mass directly, like a piezobalance, should not give this curvature since coagulation would not have any effect and  $K_k = 0$ .

Table 2.2 shows the different values obtained when fitting the experimental data. Specially notable is the case of the Ecochem PAS 2000 CE device, where the effective air exchange rate  $\Phi$  is about twice as big as the one of the other sensors, this difference may be due to the fact that the photoionization of the particles is strongly

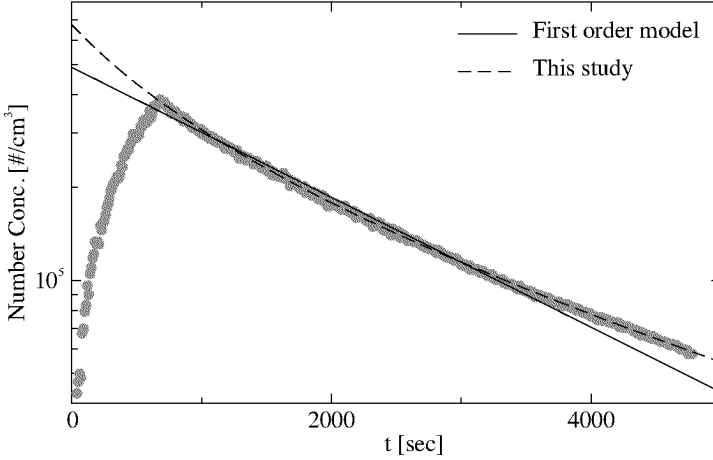


FIGURE 2.2. Fit of our model for an aerosol decay process after simultaneously burning four cigarettes compared with the fit obtained by using the linear model.

enhanced by the coverage of PPAH and therefore any chemical change on the active surface of the particle will add to the total value of  $\Phi$ .

It was previously mentioned that for the number concentration  $K_0 = K$  is the actual coagulation coefficient. Lee and Chen (1984) give an explicit equation for the average coagulation coefficient  $\bar{K}$  for lognormal distributions with  $d_p > \lambda$ .

(31)

$$\bar{K} = \frac{2kT}{3\eta} \left[ 1 + \exp(\ln^2 \sigma_g) + \frac{2.49\lambda}{\text{CMD}} [\exp(0.5 \ln^2 \sigma_g) + \exp(2.5 \ln^2 \sigma_g)] \right],$$

where  $\lambda$ , CMD, and  $\sigma_g$  are the mean free path, count median diameter and geometric standard deviation, respectively. At normal conditions, this yields for our initial size distribution (CMD= 102 nm,  $\sigma_g = 2$ )  $1.5 \times 10^{-9} \text{ cm}^3/\text{s}$  which is a factor 0.68 smaller than our fitted value of  $2.2 \times 10^{-9} \text{ cm}^3/\text{s}$ .

TABLE 2.1. Summary of the residual values obtained by using our model and the linear model.

	Dustrak	DC 2000 CE	PAS 2000 CE	CPC 3025A
<b>in absolut value<sup>a</sup></b>				
av diff	$0.19 \times 10^{-4}$	$-0.17 \times 10^0$	$-0.33 \times 10^{-1}$	$0.07 \times 10^2$
av diff lin	$-8.55 \times 10^{-4}$	$-1.47 \times 10^0$	$-2.97 \times 10^{-1}$	$-9.00 \times 10^2$
$\sigma$	$0.71 \times 10^{-2}$	$1.73 \times 10^1$	$3.06 \times 10^0$	$2.22 \times 10^3$
$\sigma_{\text{lin}}$	$1.33 \times 10^{-2}$	$2.77 \times 10^1$	$3.32 \times 10^0$	$7.57 \times 10^3$
<b>in percent<sup>b</sup></b>				
av diff	0.03	-0.06	0.19	0.05
av diff lin	-0.65	-0.41	-1.50	-2.26
$\sigma$	1.07	1.42	7.51	1.16
$\sigma_{\text{lin}}$	2.79	2.37	7.88	6.4

<sup>a</sup> The residuals values where calculated as:  $\text{residual} = x_{\text{obs}} - x_{\text{model}}$ . <sup>b</sup> The residual values in percent, where calculated as:  $\text{residual} = 100 \times (x_{\text{obs}} - x_{\text{model}}) / x_{\text{obs}}$ .

Abbreviations: av, average; diff, difference; lin, linear model; obs, observed.

TABLE 2.2. Comparison between the parameters found for the first and second order decay rate coefficients and the observed peak concentration of one of our indoor measurements for aerosol devices using different measuring principles

	Dusttrak	DC 2000 CE	PAS 2000 CE	CPC 3025A
Units	[mg/m <sup>3</sup> ]	[S.U./m <sup>3</sup> ] <sup>c</sup>	[ng/m <sup>3</sup> ]	[#/cm <sup>3</sup> ]
Property	Light scattering	Active Surface	Active Surface, Photoionization	Number Concentration
$\Phi^a$	$2.60 (\pm 0.03) \times 10^{-4}$	$3.57 (\pm 0.04) \times 10^{-4}$	$5.74 (\pm 0.08) \times 10^{-4}$	$2.85 (\pm 0.03) \times 10^{-4}$
$K_k^b$	$3.94 (\pm 0.12) \times 10^{-4}$	$7.61 (\pm 0.43) \times 10^{-8}$	$1.25 (\pm 0.14) \times 10^{-7}$	$2.21 (\pm 0.03) \times 10^{-9}$
Peak	$1.029 (\pm 0.002) \times 10^0$	$2.923 (\pm 0.004) \times 10^3$	$2.236 (\pm 0.008) \times 10^2$	$3.801 (\pm 0.005) \times 10^5$
$\frac{1}{2}K_k \times \text{Peak}$	$2.0 \times 10^{-4}$	$1.1 \times 10^{-5}$	$1.4 \times 10^{-5}$	$4.2 \times 10^{-4}$

<sup>a</sup>  $\Phi$  in air changes per second. <sup>b</sup>  $K_k$  in [1/Moment units  $\times$  sec]. <sup>c</sup> S.U. stands for surface units.

The positive value of  $K_k$  for the light scattering indicates that the Rayleigh scattering is not the dominant scattering mechanism of our aerosol sample. This is not surprising since at least 50% of our particles are too big to be described by this scattering process.

Since, as opposed to  $\Phi$ , the units of  $K_k$  depend on the units of the measured property, it is difficult to directly compare the values for the different sensors. Nevertheless, we can do a first approximation by multiplying the value  $\frac{1}{2} K_k$  by the maximum concentration (denoted as Peak) obtained in one of our indoor measurements. When doing so, we see that the coagulation has a stronger influence (up to one order of magnitude higher) in the case of the number concentration. We also see that for high aerosol concentrations  $\frac{1}{2} K_k \times \text{Peak}$  can even be larger than  $\Phi$ . This is again the case of the number concentration measurement where the aerosol coagulation dominates the first part of the decay process.

The fact that each of the used sensors depends on a different property is highlighted in figure 2.3, where a comparison between the different sensors is presented by showing their signals ratio. For instance, both the PAS 2000 CE and the DC 2000 CE sensors give a signal that depends on the active surface of the particle. By taking the photoemission-to-diffusion-charging-ratio (PE/DC) the active surface dependence disappears, leaving only information about the chemistry of the particle surface (i.e. the mean photoionization per unit active surface). In our experiment, the changes in the signal ratio are most likely produced by a first order condensational growth process, thus allowing us to fit the decay with a simple exponential.

Also the change in some physical properties can be obtained by comparing our different sensors. In the case of figure 2.3, the increasing diffusion-charging-to-number-concentration-ratio (DC/NC) also means an increasing mean active surface and therefore a growing particle size since for small particles the active surface  $S \propto d_p^2$ . It is clear that coagulation plays an important role in the grow mechanism only during the first minutes of the decay process (table 2.2). After these first minutes,

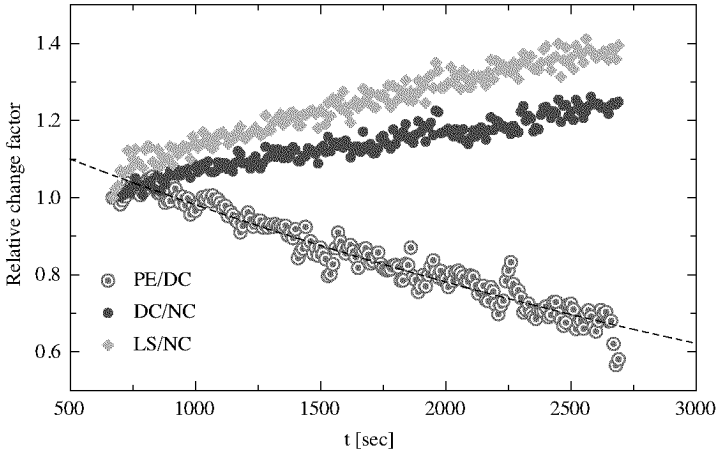


FIGURE 2.3. Change in signal ratio against time during an aerosol concentration decay process. The points represent the change in ratio of the values measured by means of photoemission (PE), diffusion charging (DC), number concentration (NC) and light scattering (LS) normalized against the signal value observed at the moment when the cigarettes burned out. The dashed curve is an exponential fit.

the constant increase in signal ratio supports our previous idea of growing process dominated by condensation. The increase in diameter is seen in the light-scattering-to-number-concentration-ratio (LS/NC) behavior as well, where the steeper LS/NC increase is due to the fact that light scattering for small particles is proportional to  $d_p^6$ .

Furthermore, by using the fact that the particle active surface  $S \propto d_p^2$  we can estimate the increase in  $d_p$  from our DC/NC data. This yields a value of  $\Delta d_p \approx 10\%$  during a 30 minutes interval for the data presented in figure 2.3. This value can be checked by analyzing the change in time of the mobility diameter distribution

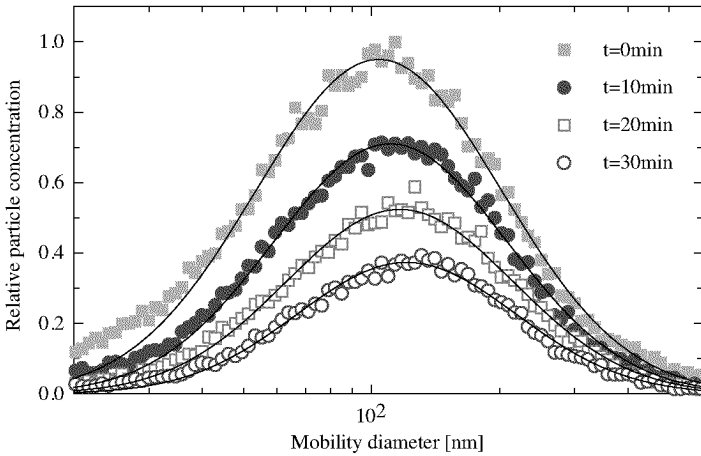


FIGURE 2.4. Size distribution spectrum of sidestream cigarette smoke observed at various times. The aerosol particles were generated by smoking 6 cigarettes with a smoking machine. The curve  $t = 0$  represents the size distribution measured just after the cigarettes burned out. The curves were fitted by assuming a lognormal size distribution.

spectrum. This is shown in figure 2.4 for a decay process of an independent measurement. By assuming a lognormal size distribution we get a change in the count mean mobility diameter of  $\Delta\bar{d}_p \approx 11\%$ , from 130 nm to 144 nm, as calculated from the fitted size distribution. This points again to an immediate field application. We can use the portable sensors to extract valuable information about the particle size spectrum without the need of doing a precise particle mobility analysis.

**4.2. Source strength determination.** One of the goals of our approach was to determine if the model with the additional nonlinear terms was suitable for calculating the amount of PPAH produced by a cigarette. For this reason a calibration of the PPAH monitors (PAS 2000 CE) was done as described in the methodology section.

The GCMS analysis of the calibration probe yielded a total of  $1.7 \mu\text{g PAH}$ , this represents a mean concentration of  $155.7 \text{ ng/m}^3$  PPAH during the 13 hours sampling period. As a comparison the same type of analysis was done to the mainstream smoke sampled extracted with the smoking machine.

By using the results obtained from the calibration and the indoor measurements technique, we used our PAS 2000 CE sensors to establish the mean emission rate of the test cigarettes, which was found to be  $8 \text{ ng/sec PPAH per cigarette}$ . This means that the total emission of one cigarette for an 11 minutes burning event would be  $5.3 \mu\text{g PPAH}$ . These results can be used to predict the PPAH concentration of a series of smoking activities. Figure 2.5 presents a comparison between such a prediction and one of our measurements. The close agreement with the experimental data shows that the method is useful to calculate the necessary air exchange rate in a room, where cigarette smoking are permitted, in order to stay below a maximum concentration. We would like to stress that even small values of the coagulation coefficient can yield a total different dynamic for highly concentrated systems when compared to the linear mass balance model. This can also be seen in figure 2.5, as we know from table 2.2 that the effect of coagulation on the PAS sensor for high concentrations is one order of magnitude smaller than in the case of the number concentration.

The same technique would allow us to calculate the total aerosol mass emission rate, called Respirable Suspended Particles (RSP), of a cigarette and to obtain the PAH-to-RSP rate. Klepeis et al. (1996) have calculated the RSP with the linear model using a piezobalance, for a different kind of cigarettes, and found it to be  $1.43 \text{ mg/min}$ . This gives us an approximated PPAH-to-RSP ratio of  $3.7 \times 10^{-4}$ . We can compare this value with the PPAH-to-TAR ratio from the mainstream smoke sampled using the smoking machine, found to be  $5.5 \times 10^{-5}$ , which shows the fact that the sidestream smoke is richer in PPAH constitution than the mainstream smoke, and with the PPAH-to-RSP ratio for traffic aerosol in the Gubrist tunnel



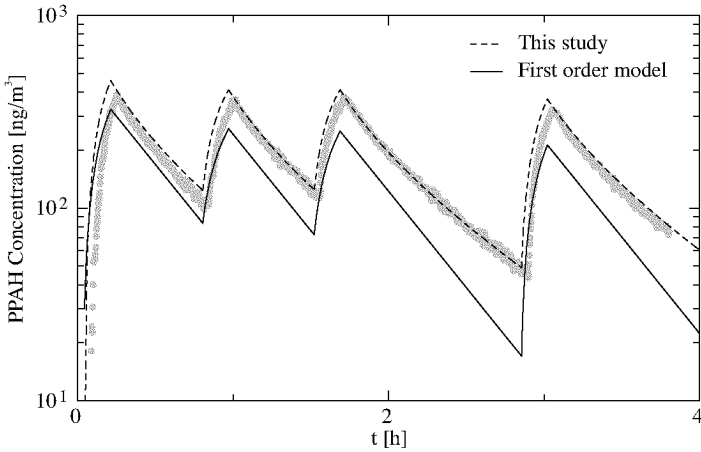


FIGURE 2.5. PPAH concentration time series measured by using a PAS 2000 CE sensor compared with the time series predicted using our model and the mass balance model ( $K_k = 0$ ). Each concentration increment represents sets of four or six cigarettes smoked at a time.

in Switzerland (Weingartner et al., 1997) determined by a chemical analysis to be  $8.6 \times 10^{-3}$  (0.86%), thus being one orders of magnitude larger than the PPAH-to-RSP ratio for sidestream cigarette smoke.



# **Magnetic circular dichroism in the photoionization of nanoparticles in gas suspension**

ABSTRACT. We present a new method capable of measuring the magnetic circular dichroism (MCD) in the photoionization of aerosol particles. This is the first device reported to be able to measure the magnetically induced optical anisotropy of nanoparticles in gas suspension. The method relies on the photoemission at energies near the threshold and is therefore sensitive to the surface magnetization. The experimental setup was tested with magnetic Ni, Co and  $\text{Fe}_3\text{O}_4$  nanoparticles. Ni showed a maximum MCD asymmetry of  $0.253 \pm 0.096\%$ , while no measurable asymmetry was detected for Co and  $\text{Fe}_3\text{O}_4$ . Further analysis with a Scanning Electron Microscope with Polarization Analysis (SEMPA) confirmed that the surface of the Co particles was magnetically inactive.

## 1. Introduction

A ferrofluid is a suspension of ultrafine magnetic particles, with typical sizes ranging from 10 to 100 nm. They play an important role in the development of technological applications, but are also used in areas of materials physics, geology, biology, and medicine. There is a lot of information available about these systems when the carrier fluid is a liquid but, to our knowledge, only a couple of studies of the magnetic properties of particles while still in gas suspension have been published (Kauffeldt and Schmidt-Ott, 1992; Kauffeldt et al., 1996; Zarutskaya and Shapiro, 2000), and none of these works focus on the magneto-optical activity of the particles.

The standard set of methods used to measure the optical properties of the ferrofluids are based in light transmission experiments. This is possible due to the relative high particle concentration that these systems exhibit. But the methods would be difficult to apply to particles suspended in a carrier gas where the diffusion losses are 100 times higher than in a liquid and therefore such high concentrations are not stable. This is probably the reason why no experimental studies of the magneto-optical properties of aerosols exist. The typical values for the volume fraction of particles in a ferrofluid,  $\phi$ , is of the order of  $10^{-2}$  and in some cases even greater than  $10^{-1}$ . As a comparison, the value of  $\phi$  for aerosol systems is usually of the order of  $10^{-13}$ .

The aim of this chapter is to present the first experimental study of magneto-optical properties of nanoparticles when still in gas suspension. The great amount of information that can be extracted by studying the photoemission of aerosol particles (Kasper et al., 1999a) together with the precedence of the study of optical anisotropy in aerosols containing organic chiral compounds (Paul et al., 1997b,a; Paul and Siegmann, 1999) suggest that the measurement of the magnetic circular dichroism in the photoionization is an ideal choice for the study of magnetic aerosol systems.

## 2. Ferrofluids

The magnetic properties of a ferrofluid are well described by the Langevin model, i.e. they exhibit a superparamagnetic behavior in the sense that they have a large saturation magnetization but their remanence magnetization is zero. By assuming a system of non-interacting monodisperse magnetic particles, the magnetization  $M$  of the particle-fluid system may be written as

$$(32) \quad M = \phi M_S L(\alpha),$$

where  $\alpha = v_p M_S H / kT$ ,  $L(\alpha) = \coth \alpha - 1/\alpha$  is the Langevin function, and  $\phi$  is the volume fraction of magnetic particles with saturation magnetization  $M_S$  and volume  $v_p$ . In the case of a polydisperse particle system the distribution function  $n(v_p)$  must be taken into account. This would yield

$$(33) \quad M = \int_0^\infty M_S v_p L(\alpha) n(v_p) dv_p.$$

Equation (33) is valid for an arbitrary distribution function as long as the particles remain non-interacting (as is normally the case for low particle volume concentration). In most cases (see for example Chantrell et al., 1978)  $n(v_p)$  can be assumed to be log-normal and is therefore given by

$$(34) \quad n(v_p) dv_p = \frac{1}{v_p \sigma_g (2\pi)^{1/2}} \exp \left[ -\frac{\ln(v_p/v_0)^2}{2\sigma_g^2} \right] dv_p,$$

where  $\sigma_g$  is the geometrical standard deviation and  $v_0$  the count mean volume of the distribution.

Most of the existing experimental studies in ferrofluids have been done in systems where the particle interaction plays a negligible role and therefore are well described by equation (33), but the case of interacting systems, in particular those where clusters and chain formation takes place, have proved to be extremely difficult to deal with. Up to now, although some experimental data is available and some empirical treatments exist, there are just a few models that approximate the behavior of

these systems for ideal cases (see for example Dormann et al., 1999, and references therein).

The ferrofluids are usually isotropic but acquire an optical anisotropy under the influence of a magnetic field. In the longitudinal Faraday's configuration (light beam parallel to magnetic field direction), the anisotropy is shown as circular birefringence and magnetic circular dichroism (MCD). Recent studies show that the dependence on the applied field of these optical properties can be directly described by the magnetization of the system: In their experimental work, Donatini et al. (1999) showed that by normalizing the value of the MCD asymmetry with its saturation value, the behaviours of the normalized curves are not altered by the change of the light wavelength used to probe the system (the same was found to be true in the case of the Faraday rotation). Moreover, Shobaki et al. (1996) found that by choosing the appropriate normalization, several magneto-optical properties for a given ferrofluid sample could be described by the same curve independently of the presence of agglomerates (where the primary particles are expected to have a strong interaction). In both cases, the curves could also be superimposed to the reduced magnetization,  $M/M_S$ , curve.

### 3. Methods

#### 3.1. Synthesis of magnetic nanoparticles in the gas phase.

3.1.1. *Nickel and Cobalt.* Nickel and Cobalt nanoparticles were produced by heating a high purity (99.9965%) metal wire with an electric current. The high temperature evaporates material from the wire and the nanoparticles are formed by condensation of the metal vapor during the subsequent cooling in a continuous flow (1.5 l/min) of a 93% N<sub>2</sub> to 7% H<sub>2</sub> gas mixture (gas purity 99.999%). The large concentration of primary particles after the condensation process leads to a high particle coagulation, thus forming agglomerates.

The produced particles are not uniform in size, they follow a lognormal size distribution, but the different aerodynamical diameter can be separated by using a differential mobility analyzer (DMA, see Knutson and Whitby, 1975). This device selects particles with the same electrical mobility (i.e. same mechanical-mobility-to-particle-charge ratio). Therefore, to guarantee that we separate only particles of a determined aerodynamical size we have to ensure that the selected particles have the same charge. This is done by attaching a diffusion charger before the DMA. The diffusion charger is a metal tube with a radioactive source inside that produces positive and negative ions that diffuse to the particles. The particles leaving the diffusion charger have a well known charge distribution (Adachi et al., 1987), most of them have a neutral charge but also positive and negative particles are produced. For particles smaller than 100 nm, the probability of multiple charging is less than 10% of that of single charging. Furthermore, this probability drops very fast as the particle cross section decreases due to the Coulomb force present in the already charged particles and only a small amount of particles with more than one charge will enter the DMA. There, the particles are separated by means of an electric field, producing a monodisperse aerosol. The particles are again neutralized with a diffusion charger and the charged fraction of the aerosol is again removed by an electric field.

The result of this process is a monodisperse aerosol containing neutrally charged metallic agglomerates, with a diameter  $d_p$  in a range of 3 to 100 nm. The technique has the disadvantage that the impurities in the wire might be incorporated in the nanoparticles.

3.1.2. *Iron oxide.* The iron oxide particles were produced using the spray pyrolysis technique. We started with a precursor solution of 13 g  $\text{Fe}(\text{NO}_3)_3 \cdot 9\text{H}_2\text{O}$  (Fluka chemika puris) in 1 liter distilled water. The solution was sprayed into the gas stream. The carrier gas was a mixture of 93%  $\text{N}_2$  to 7%  $\text{H}_2$  (gas purity 99.999%) with a flow rate of 1.5 l/min at room temperature. The gas picked up the droplets and transported them through a hot furnace (Heraeus ROF 7/50) where they were heated

at a temperature of 1050°C. The residence time in the furnace was ??? min. Under these conditions Fe<sub>3</sub>O<sub>4</sub> particles (magnetite) are most likely formed (Joutsensaari and Kaupinen, 1997).

The size distribution of the particles was again lognormal (count mean diameter 100 nm, geometrical standard deviation 1.8), and their size range was 30 to 400 nm. After the production process, a specific particle size was selected using the same technique as in the case of nickel and cobalt.

**3.2. Magnetic Filter.** We needed a method to determine if our particles were magnetic, for this we choose to reproduce the experiment reported by Kauffeldt and Schmidt-Ott (1992). The method consist of a tube filled with steel wool, which acts as a filter medium. The carrier gas with the particles flows through the filter were some particles are trapped due to diffusion to the filter fibers. The efficiency of the filter is described by its penetration,  $P$ , defined as the fraction of entering particles that exit or penetrate the filter:

$$(35) \quad P = \frac{N_{\text{Out}}}{N_{\text{In}}}.$$

By magnetizing the fibers with an external magnetic field, a strong gradient is produced in their proximity. This results in a dipole force that attracts magnetic particles towards the fibers, thus changing the value of  $P$  for such materials. The value of  $P$  can be easily determined by simultaneously measuring the particle concentration before and after the filter.

In their publication, Kauffeldt and Schmidt-Ott (1992) show that the magnetic moment of a particle  $m_p$  can be describe in terms of a given penetration, observed when magnetizing the filter fiber in a field  $H$ , as

$$(36) \quad m_p \propto \frac{\ln(P_H/P_0)}{b}.$$

Where  $P_H$  and  $P_0$  are the filter penetration values for the magnetized and non magnetized fibers respectively and  $b$  is the particle mobility.



Unfortunately, this experimental setup does not allow us to determine the absolute value of the magnetic moment. For this, we would need to calibrate the filter with particles of known magnetic moment and such a “standard” magnetic aerosol does not exist. We would also like to point out that a similar method that uses a known filter symmetry was presented by Kauffeldt et al. (1996). This method, together with the theoretical calculation that describes it (Zarutskaya and Shapiro, 2000), gives the possibility to determine on-line the absolute value of the magnetization of the suspended particles with the following restrictions: The particles have to be spherical, ferromagnetic, and single domain (the same restrictions hold for the previous study). None of these characteristics can be assumed for the particles used in our work. However, this experiment provides us a way to determine if our particles are indeed magnetic and to roughly compare their magnetic moments.

The different filter penetrations were measured for Co, Ni, and  $\text{Fe}_3\text{O}_4$  particles with mobility diameters  $d_p \in [15, 150]$  nm in fields up to 10 T. The relative magnetization was then calculated by using equation (36) for fixed values of  $H$  and, finally, a mean relative saturation magnetization was established by taking the  $\text{Fe}_3\text{O}_4$  particles as reference.

**3.3. Magnetic circular dichroism.** The experimental setup used to measure the MCD in the photoionization is shown in figure 3.1. It consists of a production part, a photoemission chamber and a detector part.

First, the aerosol particles were produced as described in the section 3.1. The neutrally charged monodisperse aerosol was directed into the photoemission chamber where it was simultaneously exposed to circular polarized light and to a constant magnetic field, parallel to the direction of the light beam, with a maximum intensity of 16 T. The high magnetic field was achieved by using a Bitter-type electromagnet from the high magnetic field facilities of the Braunschweig Technical University (HMFA-TUBS). After the photoemission chamber, the charged particles were again

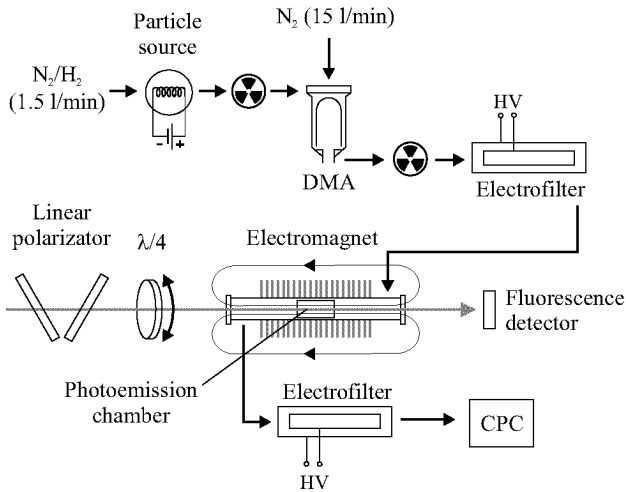


FIGURE 3.1. MCD experimental setup. The magnetic particles are generated by heating a metal wire with an electric current. The high temperature evaporates material from the wire and the nanoparticles are formed during the subsequent condensation of the metal vapor. In the DMA, only charged particles of a certain aerodynamic size are selected. The size selected particles are neutralized by a combination of a diffusion charger and an electrofilter. After this, the particles enter in the photoemission chamber where they are simultaneously exposed to a constant magnetic field and polarized light pulses. After the photoemission event, the charged particle fraction is again removed by an electrofilter and the remaining particles are counted by a CPC. A reference signal is obtained by measuring the number of particles that go through the photoemission chamber before and after the light pulses.

removed by an electric field. The remaining particles were then counted by means of light scattering using a Condensation Particle Counter (CPC, see section 3.4 for details).

The used light source was an excimer laser with a KrF gas mixture ( $\lambda = 248$  nm, pulse duration 20 ns). The laser light was first linearly polarized by a thin film polarizer and then right-handed and left-handed circular polarized light was obtained by using a rotatable  $\lambda/4$  plate. The circular polarized light was directed to a photoemission tube where it interacted with the flowing aerosol particles. The intensity of the light was chosen in such a way that 30 to 60% of the particles acquired an electrical charge through photoemission. Additionally, we used a fluorescence detector to measure the light intensity after the photoemission tube in order to monitor the intensity fluctuations from the light pulses.

The measurement was done as follows: The  $\lambda/4$  plate was set to produce a direction of circular polarized light and the laser was set to emit pulses at a frequency  $\omega$  during a time interval  $\Delta t$ . Since the charged particles are afterwards removed, the CPC will only measure the fraction of the aerosol that remains neutrally charged. The average fraction of ionized particles per laser pulse,  $n_+$  and  $n_-$ , when using right-handed and left-handed circular polarized light respectively, is given by

$$(37) \quad n_{\pm} = \frac{1}{\bar{I}\omega\Delta t} \int \left( 1 - \frac{N_{\pm}}{N_0} \right) dt,$$

where  $N_{\pm}$  is the particle concentration measured by the CPC,  $N_0$  is the background particle concentration (i.e. the particle concentration before the laser pulses), and  $\bar{I}$  is the mean light intensity of a single laser pulse. The MCD asymmetry was then determined as

$$(38) \quad A = \frac{n_+ - n_-}{n_+ + n_-}.$$

Equation (38) is valid only when  $n_{\pm} \ll 1$  (i.e. we can assume that  $n_{\pm}$  is proportional to the number of emitted photoelectrons). For a higher photoelectrical activity,

the asymmetry should be calculated by using the actual particle charge. This can be done by sampling the particles in an electrically isolated filter in combination with a current amplifier that measures the current flowing from the filter to ground potential.

## 4. Results and Discussion

**4.1. Particle properties.** As mentioned before, due to the production technique, the Ni and Co particles are mainly aggregates and their primary particles are in most cases smaller than 10 nm (figure 3.2). From the literature we know that particles in the size range of the primary particles are most likely to have single ferromagnetic domains and high coercivity or exhibit themselves a superparamagnetic behavior (see for example Morrish, 1965; Charles and Popplewell, 1980). As a contrast, the  $\text{Fe}_3\text{O}_4$  particles showed a compact spherical-like shape with almost no aggregation and, from the structure seen on their TEM images (figure 3.3), they are probably single crystals. From the interaction with the carrier gas (or with the fluid, in the case of a colloid), the surface of the particles may form an oxide, or a non-magnetic layer typically 1-2 nm thick (Kaiser and Miskolczy, 1970; Martinet, 1978; Kruis et al., 1998). This could represent a problem for our measuring technique since the photoemission only probes a layer with a thickness of a few nanometers in the case of organic compounds (Paul et al., 1995) and less than 1 nm in metals. As a result of this, a particle with a magnetic core but a magnetically inactive surface will fail to exhibit MCD.

In the case of our experiment, the use of the reductive carrier gas ( $\text{H}_2/\text{N}_2$ ) does not assure an oxide-free surface. The particle surface, or even the entire particle could oxidize. Nevertheless, Meiklejohn (1962) showed that the surface of nanoparticles of Co (see also Meiklejohn and Bean, 1956, 1957), Ni, and Fe was magnetically active even in cases where a very thick oxide layer was present (up to a 50% of the particle volume). Moreover, pure “antiferromagnetic” nanoparticles like NiO and CoO are known to exhibit superparamagnetism or even weak ferromagnetism

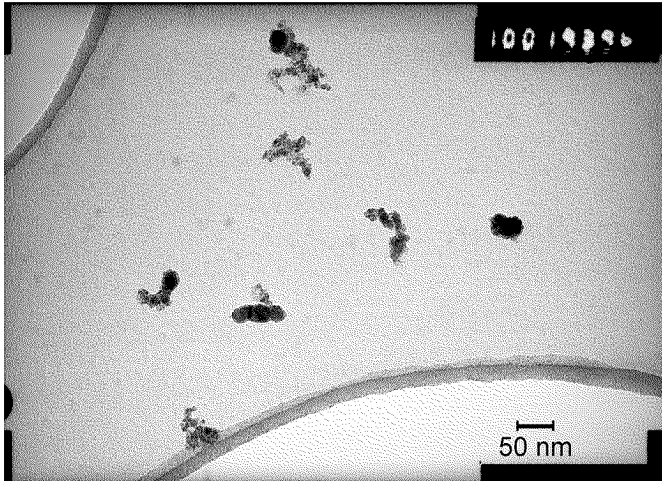


FIGURE 3.2. TEM pictures of Ni particles with a mobility diameter of 50 nm. The particles show a strong aggregation, therefore only in a few cases the mobility diameter correspond to the actual geometrical diameter. Most of the agglomerates are formed of primary particles smaller than 10 nm.

(Shuele and Deetscreek, 1962; Flipse et al., 1999). The phenomenon is thought to be a surface effect originated by the uncoupled spins at the particle surface (Shuele and Deetscreek, 1962; Kodama, 1999, and references therein). Such surface effects could be reflected in an increase of the surface magnetization in relation to the bulk in as much as 30%. What this amounts to is that the use of techniques that emphasize in the surface properties, like photoemission in the case of this study, are good candidates for the study of nanoparticles.

**4.2. Magnetic filter measurements.** All of our test particles showed indeed a decrease in the ratio of  $P_H/P_0$  as the external magnetic field was increased. This points out that the particles do possess a magnetic moment  $m$ . As mentioned before,

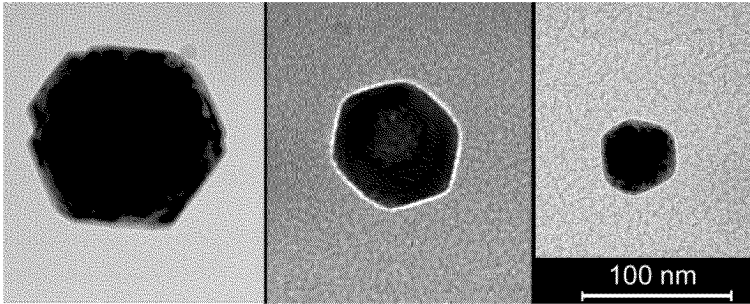


FIGURE 3.3. TEM pictures of  $\text{Fe}_3\text{O}_4$  particles of different sizes. As a contrast to the Ni and Co particles, they present a nonagglomerate spherical-like structure and are probably single-crystals.

there is no way to calibrate our measurements, thus no absolute value can be assign to  $m$ . Therefore we base our analysis in a comparison between the results found for each aerosol species. Figure 3.4 shows the results of such a comparison. There the saturation magnetization  $M_S$  of the Co and Ni particles is given as a ratio to  $M_S$  for the  $\text{Fe}_3\text{O}_4$  particles. We can see that the ratios obtained this way are larger than expected, i.e. by a factor 2.35 in the case of Ni/ $\text{Fe}_3\text{O}_4$  and 1.69 for Co/ $\text{Fe}_3\text{O}_4$ . This cannot be explained, since exactly the opposite is to be expected since agglomerates, like our Ni and Co particles, tend to have a smaller magnetic moment than nearly spherical particles like  $\text{Fe}_3\text{O}_4$  due to the interactions between their primary particles. As a matter of fact, the method tended to overestimate the magnetic moments even in the case of small  $\text{Fe}_3\text{O}_4$  particles. This point is illustrated in figure 3.5, where we present a comparison between the magnetic moment obtain from the filter measurements and the one calculated for spherical particles of the same mobility. The absolute units of the experimental measurements were obtained by using the value  $M_S = 484 \text{ kA/m}$  for the saturation magnetization of the  $\text{Fe}_3\text{O}_4$ .

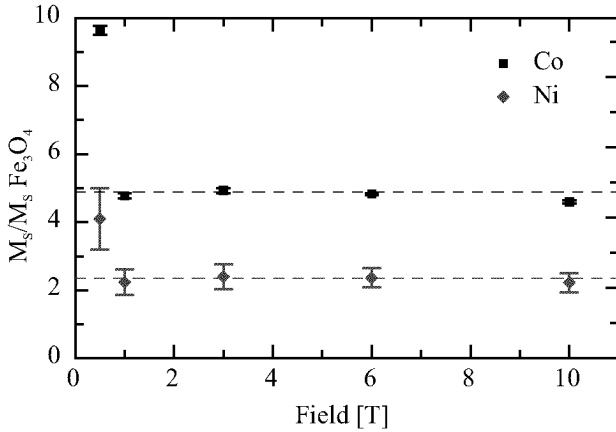


FIGURE 3.4. Estimated saturation magnetization,  $M_S$ , of Ni and Co particles as a function of the magnetic field applied to the filter. The value of  $M_S$  is expressed in terms of the  $M_S$  value found for  $\text{Fe}_3\text{O}_4$ . The dashed lines represent the mean magnetization ratio: 2.35 for Ni/ $\text{Fe}_3\text{O}_4$  and 4.89 for Co/ $\text{Fe}_3\text{O}_4$ . As a comparison, the actual ratios for spherical particles solely made of these materials would be 1 for Ni/ $\text{Fe}_3\text{O}_4$  and 2.9 for Co/ $\text{Fe}_3\text{O}_4$ .

We would like to emphasize that the magnetic filter experiment has its limitations and should in no way be used for an exhaustive discussion of the magnetic properties of aerosol particles. Nevertheless, in the case of this study, it provides us with an evidence of the magnetic nature of our aerosol samples.

**4.3. Magnetic dichroism results.** The experimental setup was tested with an aerosol made of tyrosine isomers. Tyrosine is a chiral organic compound that exhibits natural circular dichroism (NCD) in the photoionization. Paul et al. (1997b,a) and Paul and Siegmann (1999) used a similar experimental setup as the one reported

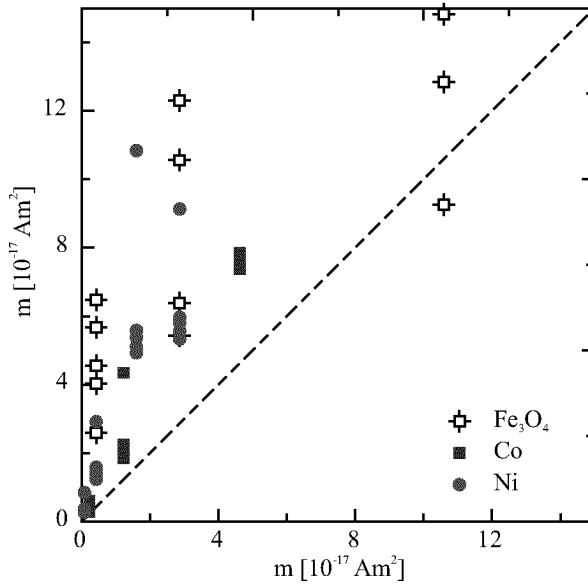


FIGURE 3.5. Magnetic moment of spherical Ni, Co, and  $\text{Fe}_3\text{O}_4$  particles vs. the magnetic moment estimated by using the magnetic filter on our aerosol sample. The absolute experimental values were obtained by assuming spherical particles and the value of 484 kA/m for the saturation magnetization of  $\text{Fe}_3\text{O}_4$ . The different experimental values for a single calculated magnetic moment correspond to measurements made with different external magnetic fields.

in this work to measure the NCD in the photoionization of aerosol samples made of the two isomers of tyrosine when still in gas suspension. They measured asymmetry values between 0.5 and 10%. The difference for the NCD-asymmetries arise from its dependence upon the crystal structure of the particle, and therefore, the crystallization time and particle size play an important role. The value of 10% corresponds to



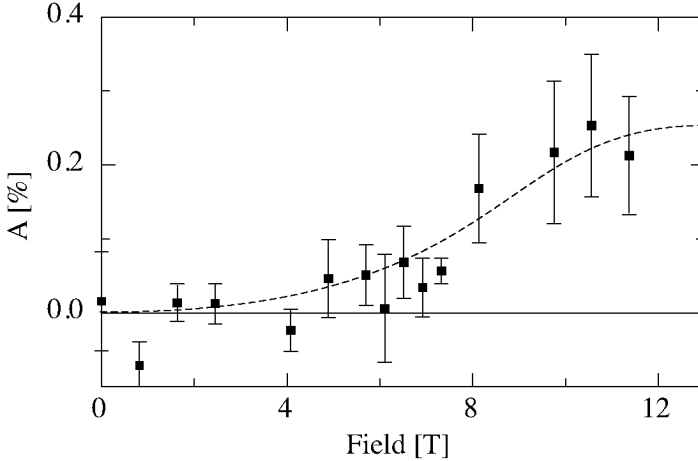


FIGURE 3.6. MCD asymmetry of Ni particles with a mobility diameter  $d_p = 50$  nm as a function of the applied magnetic field. The dashed curve is a guide to the eye.

larger particles ( $d_p = 160$  nm) with a long crystallization time, and measured with a low light intensity.

Our own measurements reported a value of  $3.25 \pm 0.31\%$  for L-tyrosine particles with  $d_p = 150$  nm. This value although smaller than the reported maximum of 10% is still surprisingly high (Paul and Siegmann, 1999) and, as mentioned before, it could be improved by a longer crystallization time. Further tests of our experimental setup yielded that it is suitable for measuring anisotropies within a statistical uncertainty as low as 0.01%.

4.3.1. *Nickel.* The MCD was then measured on the Ni sample ( $d_p = 50$  nm). The measurement yielded a maximum MCD asymmetry of  $0.253 \pm 0.096\%$ . This value was found for fields greater than 9 T. The measured dependence of the asymmetry on the magnetic field is plotted in figure 3.6. It is difficult to understand the

meaning of the results shown in this figure since they strongly diverge from the expected Langevin behavior. A possible explanation for this behavior could be the restructuring of the particle in the magnetic field.

Studies made with ferrofluids have shown that the presence or agglomerates has a strong influence in the behavior of the magnetization curve (Raşa, 2000; Taketomi et al., 1987; Rousan, 1989). Nevertheless, the existing experiments and the models for agglomerates formations (Dormann et al., 1999; Abu-Aljarayesh and Migdadi, 1999) just deal with the case where the agglomerates are formed in the presence of a magnetic field. Our aerosol is diluted enough to prevent the interactions between particles, and therefore the formation of chains is very unlikely. However, the aerosol particles themselves are already aggregates. The aggregates could be stretched in the presence of the field to a more energetically favorable shape, or could even break (Gorobets et al., 2000).

Depending upon the production process, the agglomerates could be formed by primary particles held together by relatively weak forces (probably van der Waals), or can present strongly necked primary particles held together by ionic or covalent bonds. Friedlander et al. (1998) (see also Friedlander, 2000, pp. 353-355) have studied the stretching of nanoparticles chain aggregates and found that the stretching process appears to involve two phenomena: (i) grain boundary sliding between adjacent necked particles that form the backbone of the chain and (ii) the separation and straightening of folded particle chains held together by weak forces. In the case of a weak force of the van der Waals (vdw) type only the interaction with the primary particle nearest neighbors is of importance. For two spheres of equal diameter  $d_p$ , the vdw interaction free energy is given by (Israelachvili, 1985)

$$(39) \quad \epsilon_{\text{vdw}} = -\frac{Ad_p}{24D},$$

where  $D$  is the distance of closest approach between spheres and  $A$  is the Hamaker constant which has a value  $A \in [0.4, 4] \times 10^{-19}$  J, depending on the material. For

$A = 10^{-19}$  J,  $d_p = 5$  nm, and  $D = 0.2$  nm,  $e_{\text{vdw}} \approx 10^{-19}$  J, this represents the energy needed to break a vdw bond.

Another example of aerosol restructuring can be found in Weber and Friedlander (1997). They measured the activation energy needed for restructuring Cu and Ag agglomerates and found it to be  $0.04 - 4 \times 10^{-19}$  J. They also showed that this energy is one order of magnitude lower than the one needed to break a weak bond, the explanation for this is that for a restructuring process the bonds just need to be moved and not necessarily broken. Their work also implies that at least some of the bonds between the primary particles are held together by vdw forces. As a comparison, the energy of Ni particle ( $M_S = 484$  kA/m), with a mobility diameter  $d_p = 5$  nm, aligned in the direction of a magnetic field is  $3.17 \times 10^{-20}$  J/T. Thus, the rotation of the magnetic moment of one of the primary particles would generate enough energy to move or even break a weak bond.

It is not clear how a restructuring process would affect the magneto-optical properties of our aerosol. An easy test for determining how the presence of agglomerates affects the MCD curve would be heating the aerosol particles above their melting point before they enter the photoemission chamber (unfortunately we did not test this). Another possibility that could explain the strange behavior would be a surface magnetostriction effect (Buiron et al., 1999; Szumiata et al., 1999), which can cause abrupt changes in the magnetization curve.

4.3.2. *Cobalt and iron oxide.* No MCD asymmetry was observed for the Co and  $\text{Fe}_3\text{O}_4$  aerosols. This could mean that the particles present no surface magnetization or that the MCD asymmetry for a 248 nm wavelength is smaller than the detection limit of our system. In the case of Co, the particles were also sampled on a GaAs substrate and analyzed with a Scanning Electron Microscope with Polarization Analysis (SEMPA). The SEMPA analysis confirmed that the particle surface was non-magnetic.

## 5. Conclusions

We developed an experimental method capable of measuring the magnetic circular dichroism (MCD) in the photoionization of nanoparticles in gas suspension. This is the first device reported to be able to measure the magnetically induced optic anisotropy on an aerosol sample. The main difference between our method and the traditional methods to study ferrofluids is that it focuses on the particle surface. The traditional methods are based on the anisotropy in the light transmission, thus not only light absorption but also light scattering contribute to the anisotropy value. They can also be used with systems where the particles are covered with a non-magnetic layer. Our method would not be able to measure the optical anisotropy on those systems but, on the other hand, it gives the opportunity to study the anomalous surface effects known to exist in nanoparticles, like the weak ferromagnetism exhibited by small antiferromagnetic particles, or the so called magnetic anomalies of the ferromagnetic particles covered with an antiferromagnetic layer (for example the Ni-NiO, Co-CoO, and  $\text{Fe}_3\text{O}_4\text{-Fe}_2\text{O}_3$  systems).

The experimental setup was used to measure the optical activity of Ni agglomerates with mobility diameter  $d_p = 50$  nm. The measured dependence on the magnetic field of the MCD asymmetry strongly differs from the expected Langevin behavior. The fact that the presence of agglomerates, as well as their shape, has a strong influence on the magnetization curve of a mixed fluid-particle system suggests that this strange behavior is caused by a restructuring of the aerosol in the magnetic field. Nevertheless, this hypothesis must still be tested. The most simple way to do this would be by using a non-agglomerated aerosol. No MCD asymmetry was observed for the Co and  $\text{Fe}_3\text{O}_4$  particles. In the case of Co, a SEMPA analysis confirmed that the surface of the particles was non-magnetic.

## Bibliography

- Abu-Aljarayesh, I. and Migdadi, Sh. Numerical calculations of the entropy and magnetization of magnetic fluids with chain aggregates. *J. Magn. Magn. Mat.*, 191:174, 1999.
- Adachi, M, Okuyama, K, and Kousaka, Y. Simple evaluation method of bipolar diffusion charging of aerosol-particles and its application to smoke detectors. *Aerosol Sci. Tech.*, 7(2):217, 1987.
- Ammann, M., Hanert, R., Burtcher, H., and Siegmann, H.C. Photoelectric charging of ultrafine volcanic aerosol: Detection of Cu(I) as a tracer of chlorides in magmatic gases. *J. of Geophys. Res.*, 98:551–556, 1993.
- Brauer, M., Hirtle, R, Lang, B, and Ott, W. Assessment of indoor fine aerosol contributions from environmental tobacco smoke and cooking with portable nephelometer. *J. of Expos. Anal. Environ. Epidemiol.*, pages 136–144, 2000.
- Buiron, N., Hirsinger, L., and Billardon, R. A micro-macro model for magnetostriction and stress effect on magnetization. *J. Magn. Magn. Mat.*, 196-197:868, 1999.
- Burtcher, H. Measurement and characteristics of combustion aerosols with special consideration of photoelectric charging and charging by flame ions. *J. of Aerosol Sci.*, 23:549–595, 1992.
- Burtcher, H. and Siegmann, H.C. Monitoring PAH-emissions from combustion processes by photoelectric charging. *Combustion Sci. and Tech.*, 101:327, 1994.
- Chantrell, R.W., Popplewell, J., and Charles, S.W. Measurements of particle size distribution parameters in ferrofluids. *IEEE Trans. magnet.*, 14(5):975, 1978.

- Charles, S.W. and Popplewell, J. Ferromagnetic liquids. In Wohlfarth, E.P., editor, *Ferromagnetic materials*, volume 2. North-Holland Publishing Company, 1980.
- Chüller, U., Burtscher, H., and Schmidt-Ott, A. Photoemission from small metal spheres: A model calculation using an enhanced three-step model. *Phys. Rev. B*, 38:7814, 1988.
- Donatini, F., Jamon, D., Monin, D., and Neveu, S. Experimental investigation of longitudinal magneto-optic effects in four ferrite ferrofluids in visible-near infrared spectrum. *J. Magn. Magn. Mat.*, 35(5):4311, 1999.
- Dormann, J.L., Fionari, D., and Tronc, E. On the models for interparticle interactions in nanoparticle assemblies: comparison with experimental results. *J. Magn. Magn. Mat.*, 202:251, 1999.
- Dubowsky, S., Wallace, L.A., and Buckley, T.J. The contribution of traffic to indoor concentrations of polycyclic aromatics hydrocarbons. *J. of Expos. Anal. Environ. Epidemiol.*, 9:312–321, 1999.
- Fendel, W., Matter, D., Burtscher, H., and Schmidt-Ott, A. Interaction between carbon or iron aerosol-particles and ozone. *Atmospheric Environ.*, 29:967, 1995.
- Filippov, A.V. Charging of aerosol in the transition regime. *J. of Aerosol Sci.*, 24: 423–436, 1993.
- Filippov, A.V., Schmidt-Ott, A., and Fendel, W. Escape Probability of Photoelectrons from Particles. *J. of Aerosol Sci.*, 24(Suppl. 1):S501–S502, 1993.
- Flipse, C.F.J., Rouwelaar, C.B., and de Groot, F.M.F. Magnetic properties of CoO nanoparticles. *Eur. Phys. J. D*, 9:479, 1999.
- Friedlander, S.K. *Smoke, Dust, and Haze*. Oxford University Press, 2000.
- Friedlander, S.K., Jang, H.D., and Ryu, K.H. Elastic behavior of nanoparticle chain aggregates. *Phys. Rev. Lett.*, 72(2):173, 1998.
- Fuchs, N.A. *The Mechanics of Aerosols*. Dover Publ. Inc., New York, 1964.
- Gäggeler, H.W., Baltensperger, U., Emmenegger, M., Jost, D.T., Schmidt-Ott, A., Haller, P., and Hofmann, M. The epiphaniometer, a new device for continuous

- aerosol monitoring. *J. of Aerosol Sci.*, 20:557–564, 1989.
- Gorobets, S.V., Legenkii, Y.A., and Melnichuk, I.A. Break-up of ni microparticle clusters in a magnetic field. *J. Magn. Magn. Mat.*, 222:159, 2000.
- Hinds, William C. *Aerosol Technology*. John Wiley & Son, 1982.
- Hueglin, Ch., Paul, J., Scherrer, L., and Siegmann, K. Direct observation of desorption kinetics with perylene at ultrafine aerosol particle surfaces. *J. of Phys. Chem. B*, 101:9335–9341, 1997.
- Israelachvili, J.N. *Intermolecular and surface forces*. Academic Press, 1985.
- Joutsensaari, J. and Kaupinen, E.I. *Mat. Res. Soc. Symp.*, page 457, 1997.
- Kaiser, R. and Miskolczy, G. Magnetic properties of stable dispersions of subdomain magnetic particles. *J. Appl. Phys.*, 41(3):1064, 1970.
- Kalberer, M., Ammann, M., Tabor, K., Parrat, Y., Weingartner, E., Piguet, D., Rössler, E., Jost, D.T., Türlér, A., Gäggeler, H.W., and Baltensperger, U. Heterogeneous chemical processing of (NO<sub>2</sub>)-N-13 by monodisperse carbon aerosols at very low concentrations. *J. of Phys. Chem.*, 100:15487, 1996.
- Kasper, M., Keller, A., Paul, J., Siegmann, K., and Siegmann, H.C. Photoelectron spectroscopy without vacuum: nanoparticles in gas suspension. *J. of Elec. Spec.*, 98-99:83–93, 1999a.
- Kasper, M., Sattler, K., Siegmann, K., Matter, U., and Siegmann, H.C. The influence of fuel additives on the formation of carbon during combustion. *J. of Aerosol Sci.*, 30:217–225, 1999b.
- Kauffeldt, Th., Kleinwechter, H., and Schmidt-Ott, A. Absolut on-line measurement of the magnetic moment of aerosol particles. *Chem. Eng. Comm.*, 151:169, 1996.
- Kauffeldt, Th. and Schmidt-Ott, A. On-line measurement of the magnetic moment of aerosol. *J. of Aerosol Sci.*, 23(S1):S425, 1992.
- Keller, A., Fierz, M., Siegmann, K., Siegmann, H.C., and Filippov, A. Surface science with nanosized particles in a carrier gas. *J. of Vac. Sci. and Technol. A*, 19(1):1–8, 2001.

- Klepeis, N.E., Ott, W.R., and Switzer, P. A multiple smoker model for predicting indoor air quality in public lounges. *Environ. Sci. Technol.*, 30(9):2813–2820, 1996.
- Knutson, E.O. and Whitby, K.T. *J. of Aerosol Sci.*, 6:443, 1975.
- Kodama, R.H. Magnetic nanoparticles. *J. Magn. Magn. Mat.*, 200:359, 1999.
- Kruis, F.E., Fissan, H., and Peled, A. Synthesis of nanoparticles in the gas phase for electronic, optical and magnetic applications - a review. *J. of Aerosol Sci.*, 29(5/6):511, 1998.
- Kulmala, M. Atmospheric aerosols: Global effects. *J. of Aerosol Sci.*, 30(Supl. 1): 1–2, 1999.
- Lee, K.W. and Chen, H. Coagulation rate of polydisperse particles. *Aerosol Sci. Tech.*, 3:327–334, 1984.
- Martinet, A. Biréfringence et dichroïsme linéaire des ferrofluides sous champ magnétique. *Rheol. Acta*, 13:260, 1978.
- Matter, U., Siegmann, H.C., and Burtscher, H. Dynamic field measurements of submicron particles from diesel engines. *Environ. Sci. Technol.*, 33:1946–1952, 1999.
- Meiklejohn, W.H. Exchange anisotropy - a review. *J. Appl. Phys.*, 33(3):1328, 1962.
- Meiklejohn, W.H. and Bean, C.P. New magnetic anisotropy. *Phys. Rev.*, 102(5): 1413, 1956.
- Meiklejohn, W.H. and Bean, C.P. New magnetic anisotropy. *Phys. Rev.*, 105(3): 904, 1957.
- Morrish, A.H. *The physical principles of magnetism*. John Wiley & Sons, New York, 1965.
- Ott, W. and Klepeis, N. Technical report no. 1: Development of an advanced total human exposure model. Technical report, Indoor-outdoor PAH time series from the residential exposure project., 1995.



- Ott, W., Langan, L., and Switzer, P. A time series model for cigarette smoking activity patterns: Model validation for carbon monoxide and respirable particles in a chamber of an automobile. *J. of Expos. Anal. Environ. Epidemiol.*, 2(Suppl. 2): 175–200, 1992.
- Ott, W., Wilson, N., Klepeis, N., and Switzer, P. Real-time monitoring of polycyclic aromatic hydrocarbons and respirable suspended particles from environmental tobacco smoke in a home. In *Proceedings of the international Symposium of the Air and Waste Management Association (May 1994)*, Pittsburgh, 1994. Air and Waste Management Association.
- Paul, J., Burtscher, H., and Siegmann, K. Size dependent photo emission studies on aerosols determination of the electron escape depth. *J. of Aerosol Sci.*, 26(Supl. 1):239, 1995.
- Paul, J., Dörzbach, A., and Siegmann, K. Circular dichroism in the photoionization of nanoparticles from chiral compounds. *Phys. Rev. Lett.*, 79(16):2947, 1997a.
- Paul, J., Dörzbach, A., and Siegmann, K. Detection of chirality in ultrafine aerosol. *J. of Aerosol Sci.*, 28(Suppl. 1):S319, 1997b.
- Paul, J. and Siegmann, K. Large natural circular dichroism in photoionization. *Chem. Phys. Lett.*, 304:23–27, 1999.
- Peters, A., Skorkovsky, J., Kotesovec, F., Brynda, J., Spix, C., Wichmann, H.E., and Heinrich, J. Association between mortality and air pollution in europa. *Environ. Healt*, 108(4):283–287, 2000. And references cited therein.
- Qian, Z., Siegmann, K., Keller, A., Matter, U., Scherrer, L., and Siegmann, H.C. Nanoparticles air pollution in mayor cities and its origin. *Atmospheric Environment*, 34:443–451, 2000.
- Raşa, M. Magnetic properties and magneto-birefringence of magnetic fluids. *Eur. Phys. J. E*, 2:265, 2000.
- Rogak, S.N., Baltensperger, U., and Fleagan, R.C. Measurement of mass-transfer to agglomerate aerosols. *Aerosol Sci. Tech.*, 14:447–458, 1991.

- Rosenfeld, D. Suppression of rain and snow by urban and industrial air pollution. *Sci.*, 287:1793–1796, 2000. And references cited therein.
- Rousan, A.A. Faraday rotation and chain formation in magnetic fluids. *IEEE Trans. magnet.*, 25(4):3121, 1989.
- Schleicher, B., Burtcher, H., and Siegmann, H.C. Photoelectric quantum yield of nanometer metal particles. *Appl. Phys. Lett.*, 63(9):1191, 1993.
- Schmidt-Ott, A., Baltensperger, U., Gäggeler, H.W., and Jost, D.T. scaling behavior of physical parameters describing agglomerates. *J. of Aerosol Sci.*, 21:711–717, 1990.
- Schmidt-Ott, A., Schurtenberger, P., and Siegmann, H.C. Enormous yield of photoelectrons from small particles. *Phys. Rev. Lett.*, 45(15):1284–1287, 1980.
- Sherman, E. In *III Int. Symp. on Rarefied Gas Dyn.*, volume II, pages 228–260, 1963.
- Shobaki, J., Manasreh, D., Yusuf, N.A., and Abu-Aljarayesh, I. A scaling model for the optical anisotropy in magnetic fluids: dichroism and birefringence. *IEEE Trans. magnet.*, 32(6):5245, 1996.
- Shuele, W.J. and Deetscreek, V.D. Appearance of a weak ferromagnetism in fine particles of antiferromagnetic materials. *J. Appl. Phys.*, 33(3):1136, 1962.
- Siegmann, K., Scherrer, L., and Siegmann, H.C. Physical and chemical properties of airborne nanoscale particles and how to measure the impact on human health. *J. of Molecular Structure (Theochem)*, 458:191–201, 1999.
- Szumiata, T., Żuberek, R., Gonzalez, J., Álawska-Waniewska, A., and Szymczak, H. Model of surface magnetostriction in nanostructured materials. *J. Magn. Magn. Mat.*, 203:262, 1999.
- Taketomi, S., Ukita, M., Mizukami, M., Miyajima, H., and Chikazumi, S. Magneto-optical effects of magnetic fluids. *J. Phys. Soc. Japan*, 56(9):3362, 1987.
- Weber, A.P. and Friedlander, S.K. In situ determination of the activation energy for restructuring of nanometer aerosol agglomerates. *J. of Aerosol Sci.*, 28(2):179, 1997.

- Weingartner, E., Keller, C., Stahel, W.A., Burtscher, H., and Baltensperger, U. Aerosol emission in a road tunnel. *Atmospheric Environment*, 31:451–462, 1997.
- Williams, M.M.R. and Loyalka, S.K. *Aerosol Science: Theory and practice*. Pergamon Press, 1991.
- Zarutskaya, T. and Shapiro, M. Capture of nanoparticles by magnetic filters. *J. of Aerosol Sci.*, 31(8):907, 2000.
- Zhiqiang, Q., Siegmann, K., Keller, A., Matter, U., Scherrer, L., and Siegmann, H.C. Nanoparticle air pollution in major cities and its origin. *Atmospheric Environ.*, 34: 443–451, 2000.



## Acknowledgements

First and foremost I would like to thank Prof. H.C. Siegmann for having given me the possibility to do my Ph.D. in his group. He always gave me freedom for doing my research and at the same time cared for things to be working both at the professional and personal levels.

The work at the ETH would not have been possible without the help and patience of the other persons from our research group. I would like to thank our secretary Gerda Rüegg for her kindness and for making my life at the ETH a lot more easier. I thank also Konstantin Siegmann and Uli Matter, my supervisors, not only for their support but for offering me their full time friendship.

I thank my fellow Ph.D. students, from whom I keep a lot of good memories and bad pictures: Johannes Paul, for introducing me to the world of aerosols, Karl Przybilla, for being a great back-up inside and outside of the lab, and Martin Fierz, for sharing his vision of life (just take a look at <http://www.fierz.ch>). I also thank them together with Christoph Hüglin, Georg Skillas, Markus Kasper, and Qian Zhi-qiang for their friendship.

The work of a dissertation is a lot more than just scientific. It depends upon abilities that require a lot of time and practice to master. I thank the people that contributed with their expertise, our technicians Leo Scherrer, the responsible for getting my experiment to work, and Pierre Cohn, together with the members of the mechanical and the glass-blowing workshops of the ETH.

I also appreciate the helpful comments from Heinz Burtscher, Andreas Vaterlaus, Andrey Filippov, and Wayne Ott. The discussions with all of them are now an important part of this work.

The measurements of chapter 3 were done during a half year scientific-visit to Germany. For their help during this time, I thank the people from the Braunschweig Technical University: Joachim Schoennes, Uli Barkow, Horst Simontovski, Robert Hoffmann, Tilo Lampe, and all the other members of the Institute for Semiconductors and Optics. I also thank them, together with the members of the “Burschenschaft Germania”, for the good memories and for showing me what the German hospitality is all about.

## Curriculum vitae

Alejandro Niels Keller Pérez

Born on October 25th, 1970, in Bristol, England

- 1977-1989 Pre-University studies at different schools in Mexico City and Zurich.
- 1989-1994 Studies in Physics-Engineering at the Iberoamericana University, Mexico City.
- 1994-1995 Assistant at the mathematics department, Iberoamericana University, Mexico City.
- 1995 Licentiate from the Iberoamericana University, Mexico City, with the thesis “Movimientos iónicos en el  $\text{YBa}_2\text{Cu}_3\text{O}_4$  como posible mecanismo de la superconductividad de alta temperatura.”
- 1995-1997 Systems-Consultant at IDS-Comercial, Mexico City.
- Since 1997 Teaching Assistant and Ph.D. Student at the Solid State Physics Department from the ETH Zurich.  
Scholarship holder from the Mexican National Council for Science and Technology (CONACyT).

Zurich, March 2001